American Mineralogist, Volume 105, pages 35–51, 2020

New insights into the evolution of Mississippi Valley-Type hydrothermal system: A case study of the Wusihe Pb-Zn deposit, South China, using quartz in-situ trace elements and sulfides in situ S-Pb isotopes

Kai Luo[1,2,4], Jia-Xi Zhou[1,3,4,*], Zhi-Long Huang[1], John Caulfield[4], Jian-Xin Zhao[4], Yue-Xing Feng[4], and Hegen Ouyang[4,5]

[1]State Key Laboratory of Ore Deposit Geochemistry, Institute of Geochemistry, Chinese Academy of Sciences, Guiyang 550081, China
[2]University of Chinese Academy of Sciences, Beijing 100049, China
[3]School of Resource Environment and Earth Sciences, Yunnan University, Kunming 650500, China
[4]School of Earth and Environmental Sciences, The University of Queensland, Brisbane, Queensland 4072, Australia
[5]Key Laboratory of Metallogeny and Mineral Assessment, Institute of Mineral Resources, Chinese Academy of Geological Sciences, Beijing 100037, China

Abstract

Unraveling the evolution of Mississippi Valley-type (MVT) hydrothermal system is crucial for understanding ore genesis and exploration. In this paper, we take the Wusihe Pb-Zn deposit in the western Yangtze Block (South China) as a case study, using detailed ore deposit geology, quartz in situ trace elements, and sulfides in situ S-Pb isotopes, to propose a new integrated model for the evolution of MVT hydrothermal system. Four hydrothermal stages were identified in the Wusihe ore district: (I) lamellar pyrite-sphalerite; (II) disseminated, stock-work, and brecciated sphalerite-galena; (III) massive galena, and (IV) veined calcite-bitumen. Within the most representative stage (stage II), Al concentrations in quartz (Q) increase from 8.46–354 ppm (mean 134 ppm) of Q1 to 171–3049 ppm (mean 1062 ppm) of Q2, and then decrease to 3.18–149 ppm (mean 25.4 ppm) of Q3. This trend indicates the role of acid-producing processes that resulted from sulfide precipitation and acid consumption by carbonate buffering. The occurrence of authigenic non-altered K-feldspar provides further evidence that the ore-forming fluids were weakly acidic with pH values of > ~5.5. Moreover, new bulk $\delta^{34}S$ values of sulfides (+1.8 to +14.3‰) are overall lower than those previously reported (+7.1 to +20.9‰), implying that in addition to thermochemical sulfate reduction (TSR), bacterial sulfate reduction (BSR) may play an important role in the formation of S^{2-}. In situ $\delta^{34}S$ values show a larger range (–4.3 to +26.6‰), and significantly, varies within single grains (up to +12.3‰), suggesting mixing of two isotopically distinct S^{2-} end-members produced by TSR and BSR. The diagenetic and hydrothermal early phase (stage I) sulfides were formed within a nearly closed system of BSR, whereas the formation of late phase (stage II and stage III) sulfides was caused by the input of hydrothermal fluids that promoted TSR. New galena in situ Pb isotopic ratios ($^{206}Pb/^{204}Pb$ = 18.02–18.19, $^{207}Pb/^{204}Pb$ = 15.66–15.69, and $^{208}Pb/^{204}Pb$ = 38.14–38.39) suggest that the sources of mineralizing metals in the Wusihe deposit are mainly Proterozoic basement rocks. Hence, a multi-process model (i.e., basin-mountain coupling, fluid mixing, local sulfate reduction, in situ acid-producing and involvement of black shales and carbonate sequences) was responsible for the formation of the Wusihe deposit, while S^{2-} was produced by both TSR and BSR, providing new insights into the evolution of MVT hydrothermal system.

Keywords: Quartz in situ trace elements, sulfides in situ S-Pb isotopes, MVT hydrothermal system evolution, Wusihe Pb-Zn deposit, South China

Introduction

Mississippi Valley-type deposits are named after classic districts located in the drainage basin of the Mississippi River in the central United States (Guilbert and Park 1986; Paradis et al. 2007). These deposits can form by mixing of basinal fluids of contrasting reduced sulfur and metal content, driven by gravity or tectonic stress from an adjacent orogenic belt (e.g., Durham 1966; Appold and Garven 1999; Bradley and Leach 2003). Despite a broad consensus on this model for MVT ore genesis, there are several questions that remain unanswered (e.g., Leach et al. 2005, 2010; Huston et al. 2006). One such question is how to establish a complete evolution of an MVT hydrothermal system involving the original sulfur/metal source(s), detailed constraints on acid-producing processes, and precipitation models. The other is how to explain the absence of deposits in many basins that otherwise have very similar geological histories as well-endowed basins (Wilkinson 2013), namely what role the ore-forming environments (i.e., tectonic setting, wall rock sequences) played during Pb-Zn mineralization.

The Upper Yangtze Pb-Zn metallogenic province covers an area of 170000 km^2 and contains ~400 carbonate-hosted epigen-

* E-mail: zhoujiaxi@ynu.edu.cn

0003-004X/20/0001–035$05.00/DOI: https://doi.org/10.2138/am-2020-7021

etic Pb-Zn deposits totaling ~26 Mt of metal reserves (Fig. 1a; e.g., Liu and Lin 1999; Zhou et al. 2015, 2018a). The Wusihe Pb-Zn deposit is the largest in the northwest part of the province (Fig. 1b; ~5.4 Mt grading 8.6% wt. Zn and 2.0 wt% Pb) (Xiong et al. 2018). This deposit is hosted in siliceous and evaporitic carbonate sequences of the late Ediacaran Dengying Formation, which are unconformably overlain by the early Cambrian Qiongzhusi Formation black shales (Shao and Li 1996; Xiong et al. 2018; Zhu et al. 2018). Despite the Wusihe deposit resembling MVT deposits in the central United States (Supplemental[1] Table S1; e.g., Wu et al. 2013; Xiong et al. 2018), it shows many distinctive geological and geochemical features that warrant further investigation. First, the Wusihe ore district is characterized by a ~50 km length of ore-bearing strata (Lin 2005; Li 2007), which are clearly distinct from those of classical MVT deposits. Second, large amounts of bitumen and authigenic non-altered K-feldspar have been noted in association with the Pb-Zn mineralization. And last, the ore structures within this single deposit are very complex, including lamellar, stock-work, brecciated, veined, disseminated, and massive ore types (Sverjensky 1981; Gibbins 1983).

Given these features, it has been proposed that the Wusihe deposit may have formed in a unique tectonic environment (Leach et al. 2005), which represents an ideal locality to investigate the interplay among these factors and the evolution of MVT hydrothermal system. Accordingly, to better understand how these aspects influenced Pb-Zn mineralization, we undertook a detailed study to trace the ore formation processes.

Sulfur (S) and lead (Pb) isotopes are powerful indices that can be used to trace the sources of fluids and mechanism of sulfide precipitation (e.g., Ohmoto 1986; Wilkinson et al. 2005). High spatial resolution in situ S and Pb isotopic measurements can provide vital information about the fluid origin and the nature of mineralization processes, constraints that cannot be resolved using conventional bulk analytical methods (Peevler et al. 2003; Kucha 2010; Xue et al. 2015; Zhou et al. 2018b). Furthermore, aluminum (Al) concentrations in quartz can be an effective proxy for the pH of ore-forming fluids, because they are strongly affected by Al solubility (Rusk et al. 2008; Chen et al. 2011).

Using scanning electron microscope cathodoluminesence (SEM-CL), laser ablation inductively coupled plasma mass spectrometry (LA-ICPMS) quartz in situ element analysis, bulk and nano secondary ion mass spectrometry (NanoSIMS) sulfide in situ

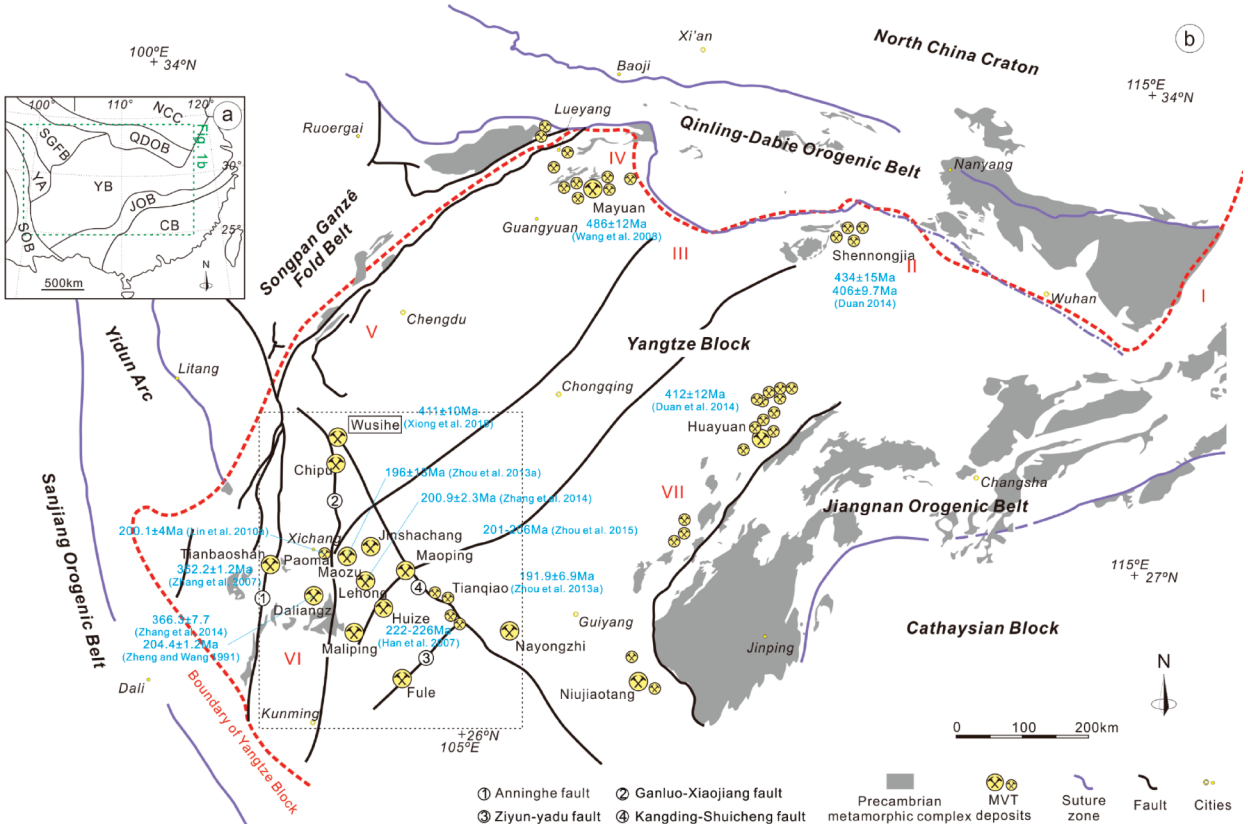

Figure 1. (**a**) Tectonic map of South China. The green dashed box (top left) indicates area shown in **b** (modified from Zhou et al. 2018b). Abbreviations: NCC = North China Craton, QDOB = Qinling-Dabie Orogenic Belt, YB = Yangtze Block, JOB = Jiangnan Orogenic Belt, CB = Cathaysian Block, SGFB = Songpan Ganzê Fold Belt, YA = Yidun Arc, SOB = Sanjiang Orogenic Belt. (**b**) Simplified tectonic map of the Yangtze block and adjacent orogenic belts with metamorphic complexes, showing distribution of MVT deposits surrounding the Yangtze Block (modified from Zhang et al. 2013; Li et al. 2018). The figure also shows (I) the Lower Yangtze northern margin; (II) the Tongbai-Dabie basin-mountain system; (III) Wudang-Dabashan basin-mountain system; (IV) Hannan-Micang multi-phased composite basin-mountain foreland deformation systems; (V) the Longmenshan intracontinental orogen foreland; (VI) the Chuxiong foreland basin, and (VII) the Qiandong-Xiangxi-E'xi orogen foreland. The black dashed box (bottom left) indicates the location of the Upper Yangtze Pb-Zn metallogenic province. (Color online.)

S isotope analysis, and femtosecond LA-Multi-collector ICPMS (LA-MC-ICPMS) galena in situ Pb isotope analysis, this study aims to: (1) evaluate the ore-forming tectonic settings and wall rock sequences; (2) trace the nature of ore-forming fluids and sulfide precipitation mechanisms; and (3) investigate the evolution of the Wusihe MVT hydrothermal system. The outcomes will contribute to a better understanding of the formation of carbonate-hosted epigenetic Pb-Zn deposits surrounding the Yangtze Block, and similar deposits globally.

Regional geology

The South China Block is made up of the Yangtze Block to the northwest and the Cathaysia Block to the southeast. The Yangtze and Cathaysia blocks were amalgamated along the Jiangnan Orogenic belt at around 820–850 Ma (Fig. 1a; e.g., Zhou et al. 2009; Wang et al. 2010; Zhao et al. 2011; Zhao 2015; Wu et al. 2018). The collision of the South China Block with the North China Craton to the north and the Indochina Block to the south occurred during the Triassic (e.g., Hou et al. 2003; Li et al. 2014; Mi et al. 2015).

The Yangtze Block consists of Mesoproterozoic basement (Fig. 1b) overlain by Neoproterozoic to Cenozoic cover sequences (Zhou et al. 2002, 2006; Zhao et al. 2010). Mesoproterozoic folded basement rocks include the ~1.7 Ga Dongchuan and ~1.1 Ga Kunyang Groups and equivalents that mainly consist of greywackes, slates, and other carbonaceous to siliceous sedimentary rocks surrounding the Yangtze Block (Wang et al. 2012). These rocks are unconformably overlain by shallow marine Paleozoic and Early Mesozoic cover sequences. Jurassic to Cenozoic strata are composed exclusively of continental sequences.

There are numerous MVT Pb-Zn districts surrounding the margin of the Yangtze Block, which are tectonically linked to basin deformation in response to orogenic activity (Fig. 1b; Wang et al. 2014; Zhang et al. 2014). Along the identified basin-mountain margins of the Yangtze Block, the early Paleozoic Qinling-Dabie basin-mountain system in the north (e.g., Lu et al. 2003; Zhang et al. 2006; Jiang et al. 2010; Wang et al. 2010) hosts the ca. 486 Ma Mayuan and ca. 434–406 Ma Shennongjia Pb-Zn deposits (Fig. 1b; e.g., Wang et al. 2008). The Jiangnan Orogenic Belt was active ca. 411–412 Ma on the southeast margin of the Yangtze Block (Fig. 1b; e.g., Chu et al. 2012), which consists of the Qiandong-Xiangxi-E'xi basin-mountain system, and hosts the ca. 412 Ma Huayuan Pb-Zn district (Fig. 1b; e.g., Duan 2014; Duan et al. 2014). Within the western margin of the Yangtze Block, the composite tectonic setting, i.e., the Xiaojiang thrust-fold, the Longmenshan intracontinental Orogenic Belt and Chuxiong foreland basins, hosts the Upper Yangtze Pb-Zn metallogenic province (Fig. 1b; Liu and Lin 1999; Zhou et al. 2013a, 2018a; Hu et al. 2017). This province contains ca. 362–411 Ma (e.g., Zhang 2008; Zhang et al. 2008, 2014a, 2014b; Wu 2013; Xiong et al. 2018) and ca. 192–226 Ma (e.g., Zhou et al. 2013b, 2015, 2018a, and references therein) Pb-Zn deposits hosted in late Ediacaran to late Permian carbonate rocks (Zhou et al. 2018b). These two age clusters correspond to the orogenic events by collision compression and post-collisional extension during late Caledonian-early Variscan (Devonian) and late Indosinian-early Yanshanian (Triassic-Jurassic), respectively (e.g., Li et al. 2006; Shu 2006).

Deposit geology

Pb-Zn deposits within the Wusihe district in the north of the Upper Yangtze Pb-Zn metallogenic province include the Heiqu-Xuequ, Hetaoping, Niuxinshan, and Wusihe deposits, all of which are hosted in late Ediacaran-early Cambrian carbonate sequences. These deposits form a large metallogenic belt along the Dadu River Valley with a length of over 50 km (Figs. 2a and 2b). Among these Pb-Zn deposits, Wusihe is the largest.

Strata

Exposed strata in the Wusihe district include Mesoproterozoic metamorphic basement and Neoproterozoic cover. The Mesoproterozoic metamorphic basement (namely the Ebian Formation) consists primarily of phyllite and is unconformably overlain by Neoproterozoic strata comprising three formations: Suxiong, Guanyinya, and Dengying. The Suxiong Formation represents a volcanic sequence containing pyroclastic deposits, tuff, and rhyolite. The Suxiong Formation is overlain by the Guanyinya Formation, which is composed of shale, limestone, and dolomite. The Neoproterozoic Dengying Formation is the most important ore-hosting unit and consists of thickly bedded cherty dolostone, with minor shales and thin (<1 m) phosphorite beds. The Lower Cambrian Qiongzusi Formation consists mainly of organic-rich black shales and is a significant source of hydrocarbons (Fig. 2c; Huang et al. 2012).

Tectonics

Faults and folds are well developed in the Wusihe mining district. The principal faults are the northwest-trending Matuo fault and the northeast-trending Wangmaoshan fault. The main fold present is the Wanlicun syncline (Fig. 2a). This tectonic framework produces secondary fault fracture zones and interlayered fault zones, which control the spatial distribution of the stratiform ore bodies.

Ore bodies

Ore bodies in the Wusihe deposit have variable thicknesses from 0.20–2.97 m, with a mean of 0.93 m. They are simple in shape, layered, extensively lentoid, and dominantly occur parallel to wall rock bedding. Ore bodies contain 0.02–14.02 wt% Pb (average 3.05 wt%), and 0.58–37.60 wt% Zn (average 12.4 wt%), and can be divided into two groups: lower and upper. The lower group of ore bodies is layered and hosted in gray siliceous dolostones. This group mainly contains sphalerite, characterized by lamellar ores with a minor disseminated component. The upper group of ore bodies is hosted in black-gray layered carbonaceous dolostone and minor black shales. The upper group occurs as layered, lens shapes, up to 14 m above the lower boundary of the Qiongzhusi Formation black shale. They are 6.3–16.3 m in thickness (mean 12.3 m), showing stock-work and disseminated ores in interlayered crushed zones, dissolution collapse structures, and brecciated ores concentrated along fault planes.

Mineralogy

At Wusihe, ores are dominantly sulfides, with lesser amounts of oxides. Mineral assemblages are comprised of both ore minerals, including pyrite, sphalerite, and galena, along with gangue minerals, including quartz, dolomite, calcite, bitumen,

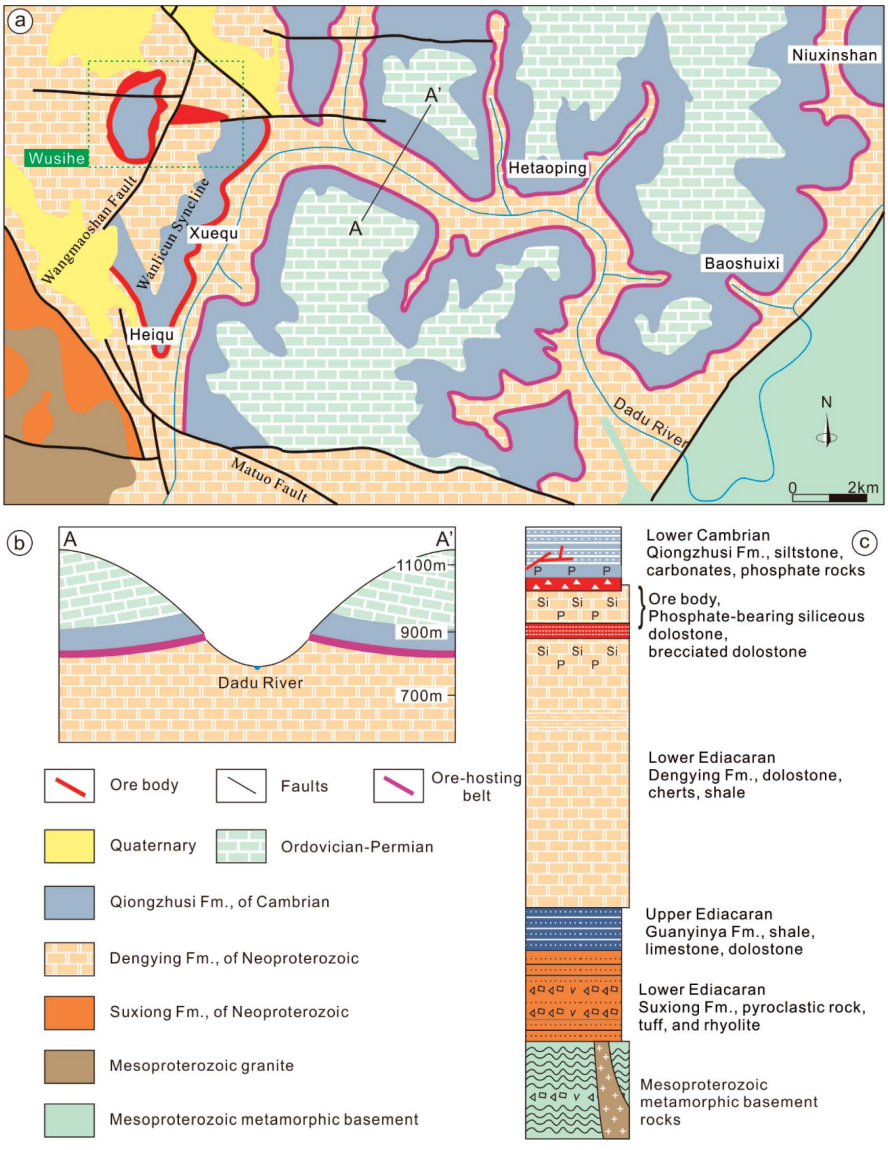

FIGURE 2. (**a**) Geological map of the Wusihe district, showing the sampling area. (**b**) Cross-section through the Wusihe district, based on drill core logging and geological mapping (modified after Lin 2005). (**c**) Schematic stratigraphic column of the Wusihe deposit (modified from Lin 2005). Legend colors are consistent with Figure 2a. Abbreviations: P = Phosphate, Si = Siliceous. (Color online.)

and potassium feldspar (Figs. 3–5). Minerals display mainly granular and colloform textures. Field observations identified six different modes of occurrence of the Pb-Zn sulfide ores in the Wusihe deposit, including lamellar, disseminated, stock-work, brecciated, veined, and massive (Fig. 3). According to the mineral assemblages and crosscutting relationships shown by the deposit, four stages of hydrothermal mineralization can be established (Fig. 6): Stage I: pyrite-sphalerite (nodules and bands of lamellar ore); Stage II: sphalerite-galena (disseminated, stockwork, brecciated ore); Stage III: galena (massive ore) and Stage IV: bitumen-calcite.

The lamellar ore typically consists of fine-grained sphalerite and pyrite horizons (several millimeter to centimeter in thickness) in carbonaceous-, siliceous- dolostone, or black shales (Fig. 3a). This ore-type is characterized by rhythmic sulfide bands, comprising yellow-, brown-, and red-colored sphalerite (60–70%), pyrite (10–20%), and minor organic matter (<10%). Structurally these bands run parallel to bedding and schistosity in the siliceous dolostone (Figs. 4a and 4b).

The disseminated ore is comprised of fine- to coarse-grained sphalerite and pyrite (0.1–10 mm). This type of ore often appears to be red-brown/light brown intergrown with light-yellow concentric rings (Figs. 3b–3f). Quartz can be divided into three generations: the first generation (Q1) occurs as euhedral hexagon grains (Fig. 5b). The second generation (Q2) is commonly subhedral coexisting with sulfides (Figs. 5c and 5d). The third generation (Q3) occurred as veinlets crosscutting sulfides or along the margins of dolomite (Figs. 5e and 5f).

The stock-work ore is composed of sphalerite and galena where sphalerite dominates (60–70%), followed by galena

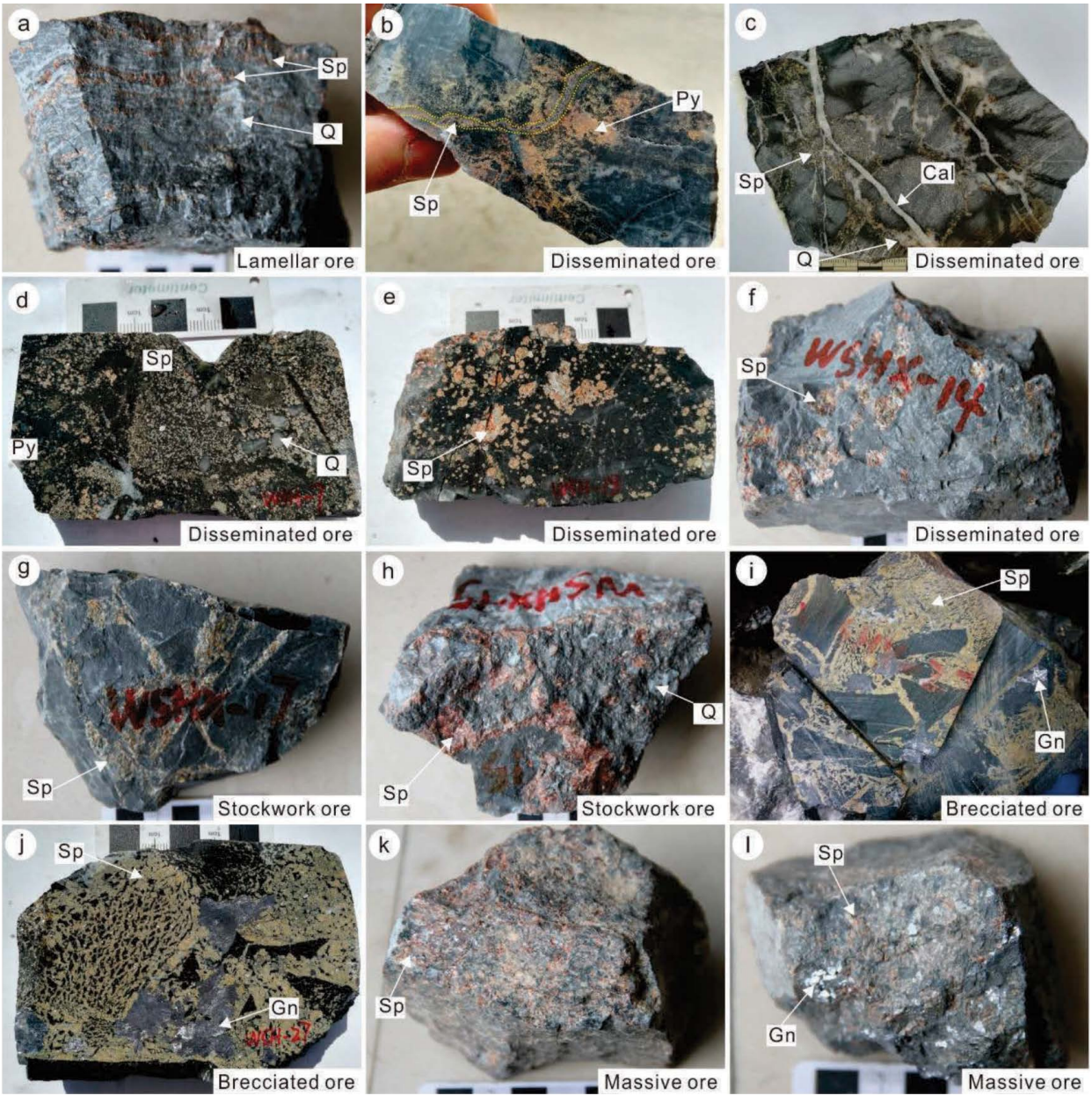

FIGURE 3. Hand specimen photographs showing different types of ores in the Wusihe deposit: (**a**) lamellar ores, (**b**–**f**) disseminated ores, (**g**–**h**) stockwork ores, (**i**–**j**) brecciated ores, (**k**–**l**) massive ores. (Color online.)

(10–20%), calcite (5–10%), quartz (1–3%), and occasional pyrite (Figs. 3g and 3h). Calcite is mainly dispersed as either blocks or short veins with a small number of occurrences along the margins of sphalerite veins (Figs. 4d and 4k). Quartz is dominantly distributed along the margins of sphalerite veins and includes large amounts of irregular bitumen (Fig. 4k).

The brecciated ore consists of sphalerite and irregular galena aggregates (Figs. 3i and 3j). They form the cement matrix to early deformation lamellar ores hosted in the siliceous dolostone. These sphalerites are predominantly yellow in color, ellipsoidal in shape, and form parallel strips with a dominant grain size of 0.5–1.2 mm. In some cases, the sphalerite occurs as single and multi-colored concentric rings (Figs. 4e–4g). Galena grains are almost square, dispersed in sphalerite grains and locally rims the sphalerite. Quartz grains are clear and coarse (0.02–0.1 cm) (Figs. 4c and 4d).

The massive ore is the highest-grade ore-type in the Wusihe deposit. It occurs as massive lodes and ore shoots 0.5 to 3 m in width. Galena is well formed and the dominant ore mineral (60–70%) followed by sphalerite (20–30%) and pyrite (10%) (Figs. 3k, 3l and 4h, 4i).

The late bitumen-carrying calcite occurs mainly as veins (Figs. 3c and 4j–4l). The calcite veins contain small amounts of sphalerite and bitumen and partially cut early quartz veins

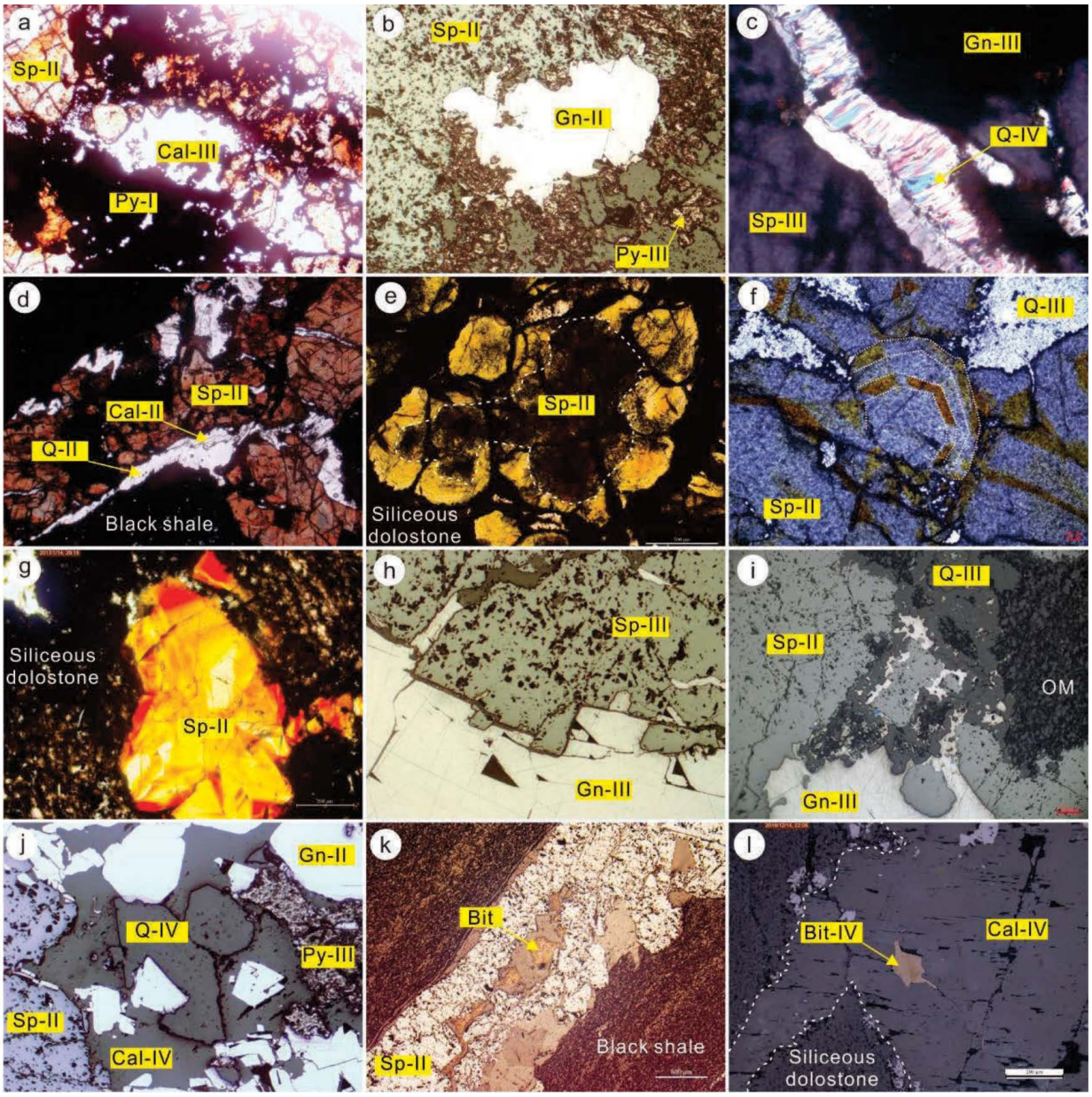

Figure 4. Photomicrographs under the microscope showing representative textures of mineral associations from different mineralization stages. (**a**) Late stage III calcite (Cal-III) infilling vugs within Sp-II and Py-I. (**b**) Late Sp-II infilling Py-I and Sp-I. (**c**) The late Q-IV veinlets with comb structure. (**d**) Brown-red Sp-II, Cal-II and Q-II infilling black shale. (**e**) Yellow colloform Sp-II enclosing a brown core. (**f**) Oscillatory-zoned Sp-II showing periodic color variations. (**g**) Mosaic Sp-II crystals in siliceous dolostone. (**h**) Gn-III coexisting with Sp-III. (**i**) Gn-III enclosing Sp-II and Py-II. (**j**) Late Q-IV and Cal-IV enclosing Gn-II, infilling Sp-II aggregates. (**k**) Stock-work ore, showing Sp-II coexisting with bitumen (Bit). (**l**) Late Cal-IV and Bit-IV infilling siliceous dolostone. Abbreviations: Cal = calcite, Sp = sphalerite, Py = pyrite, Gn = galena, Q = quartz. (Color online.)

(Fig. 3c). Quartz occurs as granular, partially fibrillar, or comb-like structures (Figs. 4c, 5e, and 5f). Quartz grains are typically 0.05–0.2 mm, occasionally reaching 0.5 mm.

Alteration

Hydrothermal alteration at Wusihe primarily consists of silicification, pyritization, and carbonatization. Alteration is mainly found in fault zones, and less commonly in the rocks hosting stratiform ore bodies. Silicification is the most pervasive alteration type in the Wusihe deposit. It mainly occurs as clear veinlets and lenses in the carbonates that are characterized by high permeability. Quartz occurs in vugs as subhedral-euhedral grains. The interior of quartz veinlets contains sphalerite and galena. Pyritization mainly occurs as irregular aggregates of fine-grained pyrite in the banded dolostone hosting lamellar ores, or disseminated pyrite intergrown with silicification or veinlets in carbonate breccias. Late, relatively weak carbonatization, is preserved as rare veinlets, and shows no genetic relationship with sulfides.

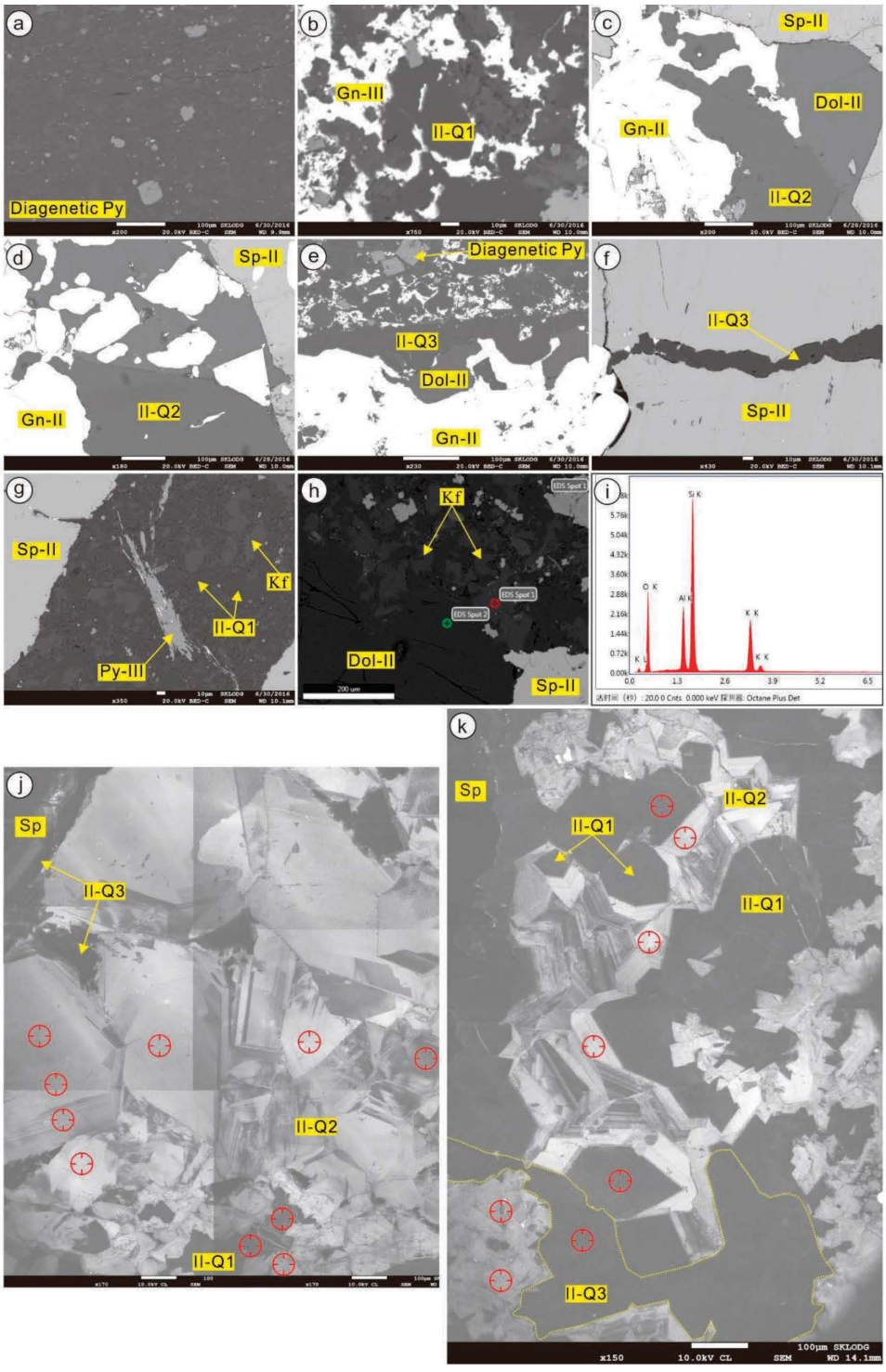

FIGURE 5. Backscattered images. (**a**) Diagenetic pyrite (Py) dispersed in siliceous dolostone. (**b**) Fine-grained euhedral-subhedral quartz (Q1) enclosed by galena (Gn-III). (**c** and **d**) Coarse-grained euhedral quartz (Q2) coexisting with dolomite (Dol-II), Gn-II and sphalerite (Sp-II). (**e**) Late anhedral quartz (Q3) occurs in veinlets infilling fractures of Gn-II and Dol-II. (**f**) Q3 occurs in veinlets infilling fractures of Sp-II. (**g**) Py-III replaced the organic matter within the original structure. (**h**) Disseminated autogenetic K-feldspar (Kf) in dolostone enclosed by sphalerite ore. (**i**) The image of energy spectra of Kf at EDS spot 1 (**h**), examined by energy-dispersive spectroscopy (EDS). (**j**–**k**) Photomosaic of a sphalerite-bearing quartz. SEM-CL image shows textual relationships of Q1–Q3 quartz crystals. Q1 is black euhedral-subhedral quartz. Q2 is later brighter quartz enclosing Q1. Q3 grew into open space, particularly along the margin of sphalerite (black mineral in upper left corner). Q3 cuts both Q1 and Q2. Red circles mark laser ablation spots of 40 μm in diameter. (Color online.)

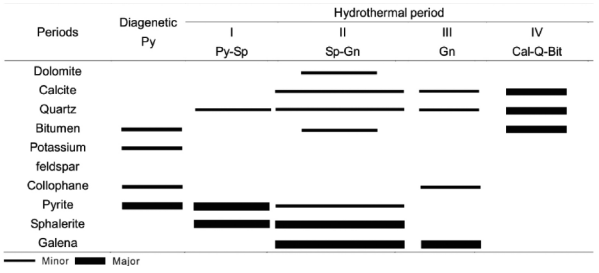

Figure 6. Schematic summary of mineral paragenesis in the Wusihe deposit. Four stages of hydrothermal mineralization include stage I (pyrite-sphalerite), stage II (sphalerite-galena), stage III (galena), and stage IV (calcite-bitumen).

Sampling and analytical methods

This study employs surface geological mapping, drill core logging, petrographic observations, and geochemical and isotopic analyses. We analyzed 24 single sulfide grains (0.4–1 mm in size) separated from the ores and 13 representative thin sections of the main mineralization stages. Twenty-four single sulfide grains were selected for bulk sulfur isotope analysis, using a Finnigan MAT-253 mass spectrometer at the State Key Laboratory of Ore Deposit Geochemistry, Institute of Geochemistry, Chinese Academy of Sciences (SKLODG-IGCAS). The precision calculated from replicated analysis of unknown samples was better than 0.2‰ (2σ). Five thin sections were imaged for SEM-CL, using JSM7800F SEM equipped with a Mono CL4 detector at the SKLODG-IGCAS. Two thin sections were selected for LA-ICPMS in situ trace element analysis of quartz from the most representative mineralization stage (stage II). Analyses were conducted at the SKLODG-IGCAS, using an Agilent 7900 ICP-MS equipped with a GeoLasPro 193 nm ArF excimer laser. The uncertainties on Li, Na, Mg, Al, K, Ti, and Ge measurements are less than 6%. Four thin sections were selected for NanoSIMS in situ analysis of S isotopes in pyrite and sphalerite. They were acquired on a CAMECA NanoSIMS 50 L at the Key Laboratory of Earth and Planetary Physics, Institute of Geology and Geophysics, CAS. The analytical precision calculated from replicated analysis of unknown samples is better than 0.2‰ (1σ). Four thin sections were analyzed using a femtosecond LA-MC-ICPMS setup for in situ analysis of Pb isotopes in galena. The analyses were conducted using a Nu II MC-ICP-MS (Nu Instruments, Wrexham, U.K.) combined with a 193 nm RESOlution M-50 femtosecond (fs) laser ablation system (ASI) at the State Key Laboratory of Continental Dynamics, Northwest University, China. Repeated analyses of NIST SRM 610 glass standard yielded highly reliable and reproducible results during the entire analytical session with mean $^{206}Pb/^{204}Pb$, $^{207}Pb/^{204}Pb$, and $^{208}Pb/^{204}Pb$ ratios of 17.052 ± 0.003, 15.515 ± 0.003, and 36.980 ± 0.007 (1SD, n = 183), respectively. Detailed analytical methods for in situ quartz trace element analysis, bulk S and in situ S-Pb isotopes are included in Appendix[1] 1.

Table 1. Bulk S isotopic composition of sulfides from the Wusihe Pb-Zn deposit

Sample no.	Mineral	Texture	Structure (stage) & color	$\delta^{34}S$ (‰)
WSH-27	Gn	Fine-grained	Brecciated (2)	+11.3
WSH-07	Gn	Coarse-grained	Disseminated (2)	+8.0
WSH-16	Gn	Fine-grained	Disseminated (2)	+3.4
WSH-23	Gn	Fine-grained	Disseminated (2)	+2.9
WSH-24	Gn	Coarse-grained	Disseminated (2)	+7.2
WSH-03	Gn	Coarse-grained	Massive (3)	+12.1
WSH-04	Gn	Coarse-grained	Massive (3)	+11.5
WSH-26	Gn	Fine-grained	Massive (3)	+1.8
WSH-22	Gn	Fine-grained	Stock-work (2)	+3.4
WSH-26	Py	Fine-grained	Massive (3)	+8.6
WSH-28	Py	Fine-grained	Massive (3)	+10.9
WSH-30	Py	Coarse-grained	Massive (3)	+10.8
WSH-34	Py	Coarse-grained	Massive (3)	+8.6
WSH-35	Py	Coarse-grained	Massive (3)	+10.5
WSH-27	Sp	Fine-grained	Brecciated (2); Yellow	+14.3
WSH-16	Sp	Fine-grained	Disseminated (2); Brown-red	+9.0
WSH-23	Sp	Fine-grained	Disseminated (2); Brown	+10.8
WSH-24	Sp	Coarse-grained	Disseminated (2); Brown	+10.4
WSH-03	Sp	Coarse-grained	Massive (3); Brown-red	+14.0
WSH-26	Sp	Fine-grained	Massive (3); Brown-red	+8.5
WSH-28	Sp	Fine-grained	Massive (3); Brown-red	+12.7
WSH-34	Sp	Coarse-grained	Massive (3); Red	+9.4
WSH-35	Sp	Coarse-grained	Massive (3); Red	+12.5
WSH-22	Sp	Fine-grained	Stock-work (2) Brown	+5.8

Note: Gn = galena; Py = pyrite; Sp = sphalerite.

Results

Stage-II is the most representative phase. Al concentrations increase from 8.46–354 ppm (mean 134 ppm; n = 8) in Q1 to 171–3049 ppm (mean 1062 ppm; n = 38) in Q2, and then decrease to 3.18–149 ppm (mean 25.4 ppm; n = 24) (Supplemental Table S1). Clear linear correlations are observed among Li, Na, and K vs. Al contents in quartz (Figs. 7a–7c). The results of bulk sulfur isotope measurements are summarized in Table 1 and are shown in Figures 8a and 9b. Bulk $\delta^{34}S$ values range from +1.8‰ to +14.3‰ (n = 24). The overall range of in situ $\delta^{34}S$ values at the micro-scale in pyrite and sphalerite grains is from –4.3‰ to +26.6‰ (Table 2), which is larger than the range of bulk sulfides (+1.8 to +14.2‰; Figs. 8b, 9a, and 9c) and includes some of the lowest (negative) values ever reported. The in situ $\delta^{34}S$ values of diagenetic pyrite vary from +23.4‰ to +24.4‰ (n = 4), those of stage I sulfides range from +16.5‰ to +26.6‰ (n = 12), and those of stage II and stage III range from +0.1 to +11.8‰ (n = 8) and –4.3 to +12.3‰ (n = 14), respectively (Fig. 10). Galena in situ Pb isotopic ratios are presented in Supplemental[1] Table S2 and are shown in Figure 11. Galena grains have the following in situ Pb isotopic ratios: $^{206}Pb/^{204}Pb$ = 18.02–18.19, $^{207}Pb/^{204}Pb$ = 15.66–15.69, and

Table 2. In situ S isotopic composition of sulfides from the Wusihe Pb-Zn deposit

Sample no.; Ore structure (stage)	Mineral	Spot location	Analysis spot	$\delta^{34}S$ (‰)
WSH-07; Fine-grained, disseminated (Diagenetic)	Py		WSH-07-01	+24.4
			WSH-07-02	+24.4
			WSH-07-03	+23.9
			WSH-07-04	+24.4
WSH-36; Fine-grained lamellar (1)	Py		WSH-36-01	+19.3
			WSH-36-02	+19.5
			WSH-36-03	+16.5
			WSH-36-04	+16.8
			WSH-36-05	+19.0
			WSH-36-06	+19.1
			WSH-36-07	+18.0
			WSH-36-08	+18.4
			WSH-36-09	+21.0
			WSH-36-10	+21.6
			WSH-36-11	+26.6
			WSH-36-12	+26.1
WSH-23; Fine-grained, disseminated (2)	Sp	Rim	WSH-23-01	+8.1
		Rim	WSH-23-02	+8.4
		Core	WSH-23-03	+0.1
		Core	WSH-23-04	+0.1
	Py	Rim	WSH-23-09	+11.3
		Rim	WSH-23-10	+11.8
		Core	WSH-23-06	+7.5
		Core	WSH-23-05	+6.9
WSH-20; Coarse-grained, massive (3)	Sp	Rim	WSH-20-01	+12.0
		Rim	WSH-20-02	+12.3
		Rim	WSH-20-03	+11.7
		Rim	WSH-20-04	+11.9
		Core	WSH-20-07	+0.0
		Core	WSH-20-08	+0.1
	Py	Rim	WSH-20-09	+1.9
		Rim	WSH-20-10	+2.3
		Rim	WSH-20-11	+3.0
		Rim	WSH-20-12	+3.7
		Core	WSH-20-13	+0.8
		Core	WSH-20-14	+1.8
		Core	WSH-20-15	–3.5
		Core	WSH-20-16	–4.3

Note: Py = pyrite; Sp = sphalerite.

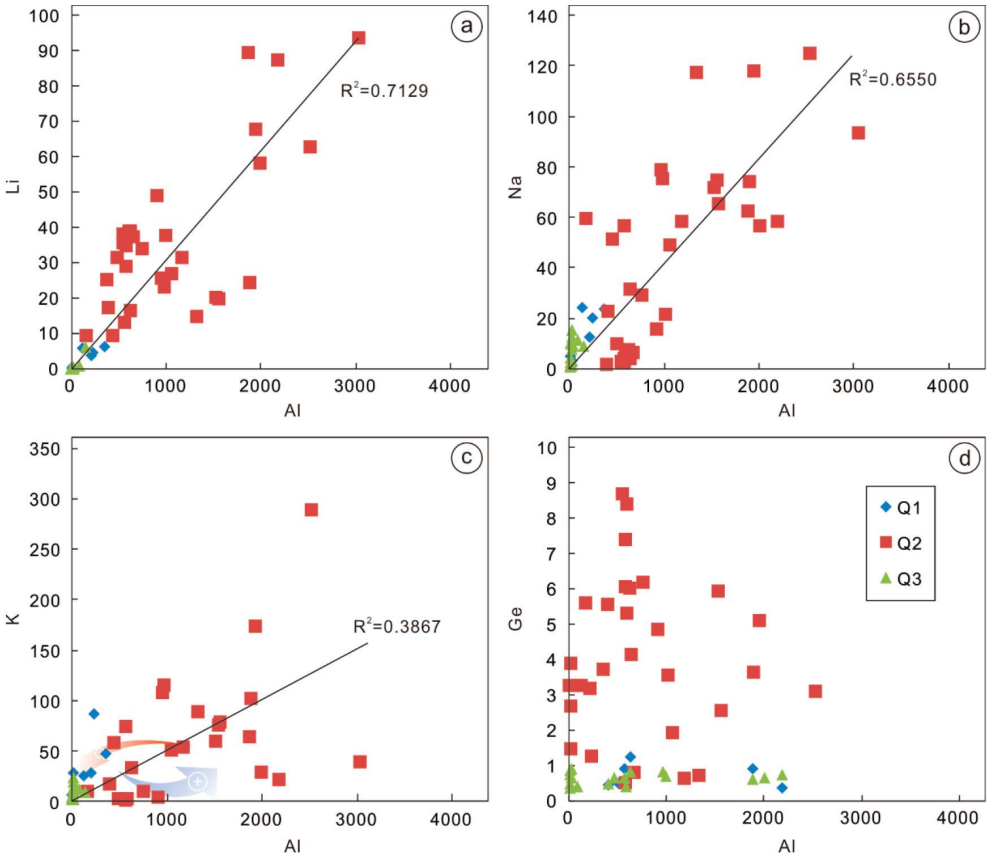

FIGURE 7. Concentrations of Li, Na, K, and Ge vs. Al (ppm) in quartz from the Wusihe deposit. Reasonable linear correlations on plots of Li, Na, and K vs. Al (ppm) are shown by the quartz data, Li vs. Al (R^2 = 0.7129), Na vs. Al (R^2 = 0.6550), and K vs. Al (R^2 = 0.3867), suggesting that compensated substitution mode (Al^{3+}+H^+/Li^+/Na^+/K^+→Si^{4+}) governing the incorporation of quartz trace elements at Wusihe. No clear linear correlation is observed on a plot of Ge vs. Al, indicating that single substitution mode (Ge^{4+}→Si^{4+}) can be ruled out (Huttenlocher 1935). Al concentrations initially show a general increase (blue arrow) from Q1 to Q2, and then to become more depleted (red arrow) in Q3. This trend suggests the variations of Al solubility in the hydrothermal fluid and indicates the role of acid-producing process resulted from sulfide precipitation, and acid consumption by carbonate buffering. (Color online.)

$^{208}Pb/^{204}Pb$ = 38.14–38.39, with μ ($^{238}U/^{204}Pb$) values of 9.63–9.67 (n = 36). Full details of in situ trace element data, bulk S, and in situ S and Pb isotopes are included in Appendix[1] 2.

DISCUSSION

Acid-producing processes

The dark-gray Q1 quartz occurs as euhedral-subhedral grains, enclosed by Q2, which is characterized by euhedral oscillatory growth zones showing variable CL intensity. Q3 dark anhedral quartz veins cut the former two generations of quartz. These complex CL textures are considered to reflect the wide range of physical and chemical conditions under which hydrothermal quartz forms (Götze and Möckel 2012).

In quartz, compensated substitution (Al^{3+}+H^+/Li^+/Na^+/K^+→Si^{4+}) is one of the key substitution modes governing the incorporation of structural trace elements (Mackey 1963; Götze et al. 2001, 2004). Of the trace elements in quartz from the Wusihe deposit, Li, K, and Na generally increase from Q1 to Q2, and then decrease in Q3 veins through time. Reasonable linear correlations between Al and these monovalent cations provide evidence for a component of coupled substitution in quartz where Al^{3+} and Li^+, K^+, or Na^+ substitute for Si^{4+} (Figs. 7a–7c). This suggests that the observed CL intensity variations may represent variations in the concentrations of Al and associated monovalent cations. Therefore, compensated substitution appears to be an important mechanism for the incorporation of Al into the quartz lattice in the Wusihe deposit.

Factors influencing Al concentrations in low-temperature hydrothermal quartz include temperature, growth rate, and aqueous Al concentration that is strongly influenced by Al solubility and pH in hydrothermal systems (Perny et al. 1992; Rusk et al. 2008; Götze and Möckel 2012). Sharp contrasts in Al concentration from zone to zone in single quartz grains from the Wusihe deposit, where no evidence for a temperature change exists, suggest that Al zoning in quartz does not result from temperature fluctuations. Crystal growth rate can also be ruled out, because in most samples, even where Al concentrations change by two orders of magnitude, no change in quartz morphology is observed (Rusk et al. 2008). Hence, Al concentrations in hydrothermal quartz from the Wusihe deposit likely reflect Al solubility and pH changes.

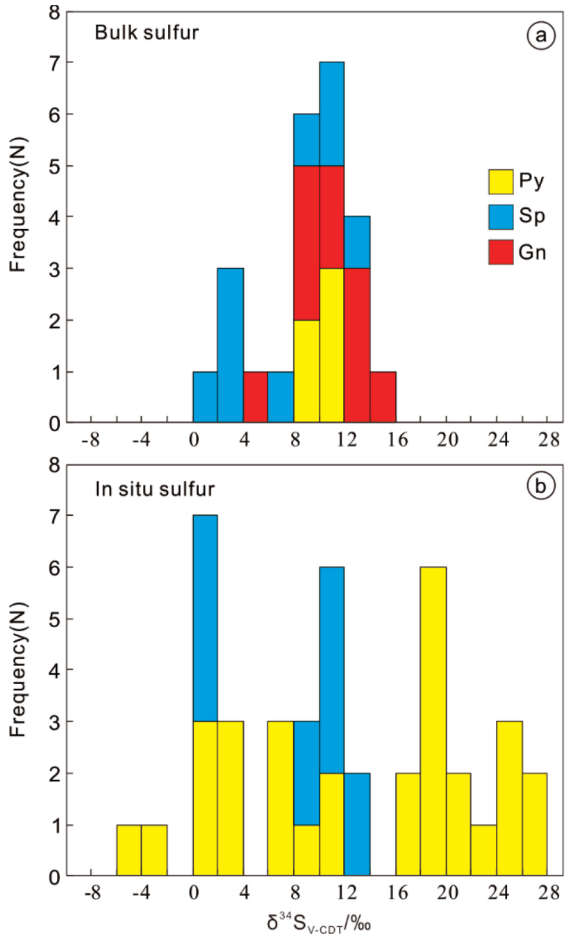

FIGURE 8. Histogram showing sulfur isotope compositions of sulfide minerals. (**a**) Bulk sulfur isotopic results. (**c**) In situ sulfur isotopic compositions. In situ $\delta^{34}S$ values measured in this study span an overall larger range compared to bulk $\delta^{34}S$ values. (Color online.)

At Wusihe, Al concentrations in Q2 can reach 3049 ppm, suggesting that the quartz precipitated from Al-enriched acidic ore-forming fluids (Rusk et al. 2008). The sharp contrast in Al concentrations from early Al-depleted quartz to late dominant Al-rich quartz reflects acidification of neutral fluids led by sulfide precipitation (Rusk et al. 2008; Chen et al. 2011). This process is consistent with reaction 1:

$$ZnCL_4^{2-}\,(aq) + H_2S\,(aq) = ZnS\,(s) + 2H^+ + 4Cl^- \quad (1)$$

(Crerar et al. 1985; Talluri 2000; Leach et al. 2005; Hammerli et al. 2015). In Figures 5j and 5k, the observed grayscale oscillatory zoning of Q2 may indicate that acid release was continuously buffered by dissolving carbonate wall rocks via reaction 2:

$$CaCO_3\,(s) + 2H^+ = Ca^{2+} + H_2CO_3\,(aq). \quad (2)$$

This reaction could facilitate solution collapse, providing space for further sulfide precipitation (Anderson and Macqueen 1982).

Furthermore, extensive SEM examination of authigenic K-feldspar (which preceded sphalerite growth, Figs. 5d–5f) in ore samples did not reveal any evidence of alteration to sericite (muscovite) and kaolinite. Such alteration would be expected if the ore fluids had pH values < ~5–5.5 at 200 °C (The homogenization temperature of fluid inclusions in sphalerite from the Wusihe deposit: 120–260 °C; Supplemental[1] Fig. S1; Jones 1993; Rusk et al. 2008; Xiong et al. 2016). Therefore, this evidence suggests that the ore-forming fluids in the Wusihe deposit were weakly acidic.

Source of sulfur

Bulk $\delta^{34}S$ values measured in this study span an overall smaller range compared to those previously reported for the Wusihe deposit ($\delta^{34}S$ = +7.1 to +20.9‰; Lin 2005; Li 2007; Xiong et al. 2018; Zhu et al. 2018). On the one hand, in agreement with previous results (Xiong et al. 2018; Zhu et al. 2018), the ^{34}S-enriched sulfides in this study ($\delta^{34}S$ = +5.8 to +14.3‰) are indicative of products of marine evaporite minerals ($\delta^{34}S_{sulfate}$ = +30.4‰ to +35.3‰; Zhou et al. 2015, 2018c; Kong et al. 2017; Yuan et al. 2017) by thermochemical sulfate reduction (TSR). The majority of fluid inclusions from the Wusihe deposit contain H_2S and CH_4 released by the thermal degradation of organic matter (Xiong et al. 2016). Accordingly, subordinate contributions of thermal degradation of organic matter (TDO) in sedimentary rocks cannot be excluded (e.g., HR_xCH_2-S-H = $R_xCH2 + H_2S$; R_x represents a large organic molecule) (Fig. 9a; Ohmoto 1972; Leventhal 1990). Conversely, the presence of lower $\delta^{34}S$ values ($\delta^{34}S$ < 5‰) in this study suggests that the sulfur in the Wusihe deposit may be derived from additional reservoirs (Fig. 9a). Possibilities include (1) H_2S from the basement granitic rocks or pyroclastic rocks ($\delta^{34}S$ = –5 to +5‰; Ohmoto and Rye 1979), and (2) H_2S formed by bacterial sulfate reduction (BSR) (Fig. 9a; Jorgensen et al. 1992).

The presence of ^{32}S-enriched sulfides may reflect fluids moving through underlying Mesoproterozoic igneous basement or the Neoproterozoic Suxiong Formation igneous rocks. However, there is almost no evidence for leaching (e.g., field observations, C-O isotopes and REE patterns) of these igneous rocks within the Wusihe district (e.g., Zheng 2012; Xiong et al. 2018; Zhu et al. 2018). Hence, igneous rocks are unlikely to contribute sulfur to the ore-forming fluid.

Open-system BSR can produce ^{32}S-enriched H_2S with a wide range of isotope fractionation (40–60‰) (Fig. 9a; Basuki et al. 2008). The biogenic H_2S mixed with H_2S produced by TSR may be the source of the lower $\delta^{34}S$ obtained in this study. The organic-enriched Qiongzhusi Fm. (black shales) could potentially serve as a reducing agent (e.g., $4R_x\text{-}CH_3 + 3SO_4^{2-} + 6H^+ = 4R_x\text{-}COOH + 4H_2O + 3H_2S$) (Leventhal 1990; Machel et al. 1995; Zhang et al. 2010; Wu 2013).

Variation of S isotopes

An increasing number of studies have shown that microscale variations in sulfur isotopic ratios obtained by in situ analysis of sulfur-bearing minerals can provide constraints on the mineralizing process that cannot be resolved from bulk $\delta^{34}S$ values alone (Peevler et al. 2003; Xue et al. 2015). This is because traditional sampling techniques such as micro-drilling or mineral separation used to obtain sulfur isotopic compositions greatly exceed the observed scale of textual variation (μm) in pyrite and sphalerite

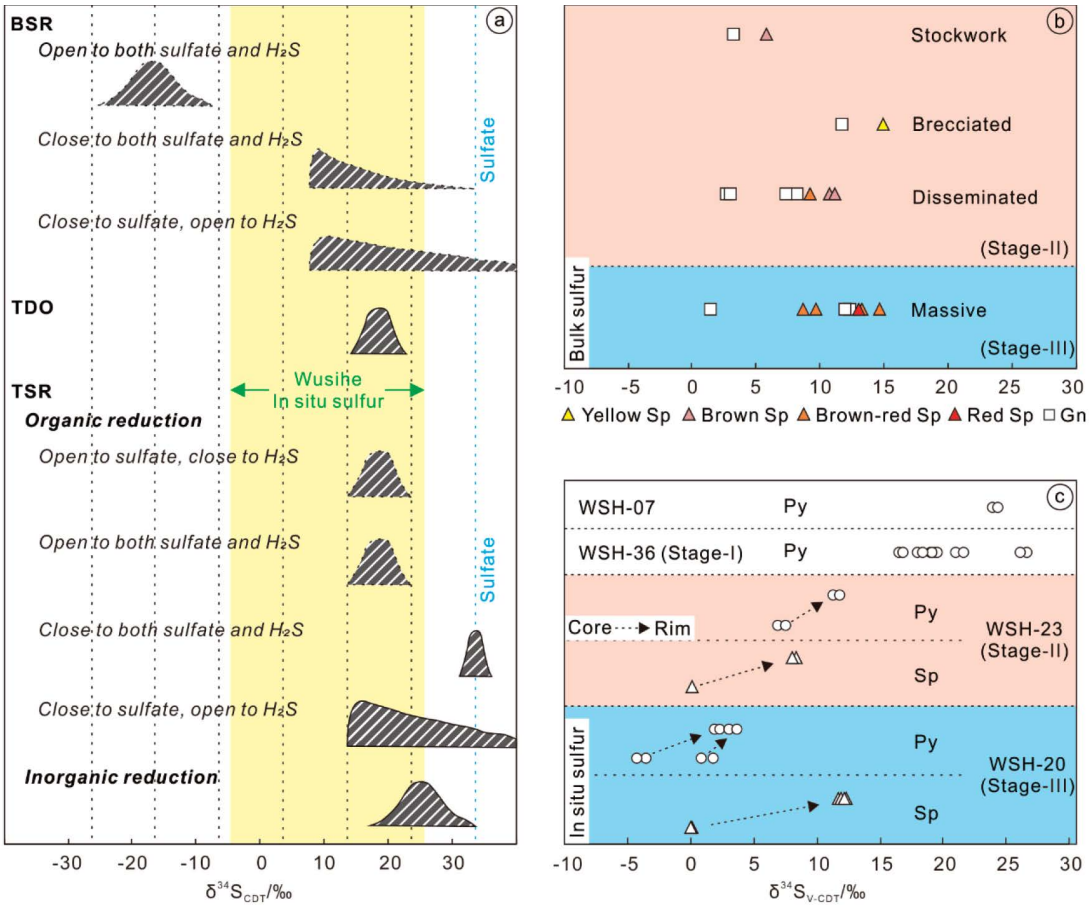

Figure 9. (**a**) Distribution pattern of $\delta^{34}S$ values for H_2S and sulfide minerals when sulfate of $\delta^{34}S$ = 33.5‰ (average value of $\delta^{34}S$ values 30.4–33.9‰ of marine barites within the Ediacaran strata in the Upper Yangtze Pb-Zn metallogenic province; e.g., Zhou et al. 2015, 2018c; Kong et al. 2017; Yuan et al. 2017) is reduced by various mechanisms (modified after Ohmoto and Rye 1979). Yellow shaded area represents in situ $\delta^{34}S$ sulfide values in the Wusihe deposit. TDO = thermal degradation of organic matter. (**b**) Distribution of bulk $\delta^{34}S$ values of different colors and types of ores in the Wusihe deposit. (**c**) Distribution of in situ $\delta^{34}S$ values of different colors and types of ores in the Wusihe deposit. Results clearly show that microscale $\delta^{34}S$ values increase from core to rim. (Color online.)

(Xiong et al. 2018; Zhu et al. 2018).

Microscale analysis shows that the variation of $\delta^{34}S$ within a thin section is small (+0.5‰: +23.9 to +24.4‰) in diagenetic samples, e.g., WSH-07, suggesting that diagenetic pyrite formed with no significant sulfur isotopic fractionation. Considerable microscale variation exists among different grains in the lamellar pyrite (variation = +8.6‰: range = +18.0 to +26.6‰) and even within single sphalerite grains in the massive ore (+12.3‰: +0.0 to +12.3‰) (Figs. 10k and 10l). To better understand the large variation of $\delta^{34}S$ values at the single grain-scale within the Wusihe deposit, the parameters affecting sulfur isotope signatures need to be evaluated.

Factors affecting the sulfur isotope signature of hydrothermal sulfide minerals include T, pH, and f_{O_2} of the fluids as well as the $\delta^{34}S$ composition of the H_2S responsible for precipitating sulfide phases. As mentioned previously, fluid inclusion homogenization temperatures in the Wusihe deposit span a considerable range (120–260 °C; Xiong et al. 2016), indicating appreciable temperature fluctuation during the course of sulfide precipitation. Temperature, however, is unlikely to have been a significant factor in producing the observed $\delta^{34}S$ variations, because sulfur isotopic fractionation between H_2S and ZnS/FeS_2 is insignificant and virtually independent of temperature (Supplemental[1] Fig. S2). Furthermore, there is almost no evidence that pyrite and barite coexist in the Wusihe deposit, even though the Ba contents of fluid inclusions obtained by LA-ICPMS are high and span a range of 281–924 ppm (Li et al. unpublished data). Calculations presented by Ohmoto (1972) suggest that outside the pyrite-barite field, changes in pH and f_{O_2} would produce only very small variations in sulfide $\delta^{34}S$ (Supplemental[1] Fig. S3) Thus, the observed variations in $\delta^{34}S$ appear to have been controlled predominantly by the $\delta^{34}S$ composition of H_2S during sulfide deposition.

The $\delta^{34}S$ of stage I pyrite is close to that of diagenetic pyrite and higher than that of stages-II and stages-III grains, suggesting that stage I pyrite formed through nearly close-system BSR with no significant fractionation (Fig. 9a). Microscale variations in sulfur isotopes show an increasing trend of $\delta^{34}S$ values from core to rim in stage II and stage III pyrite and sphalerite (Figs.

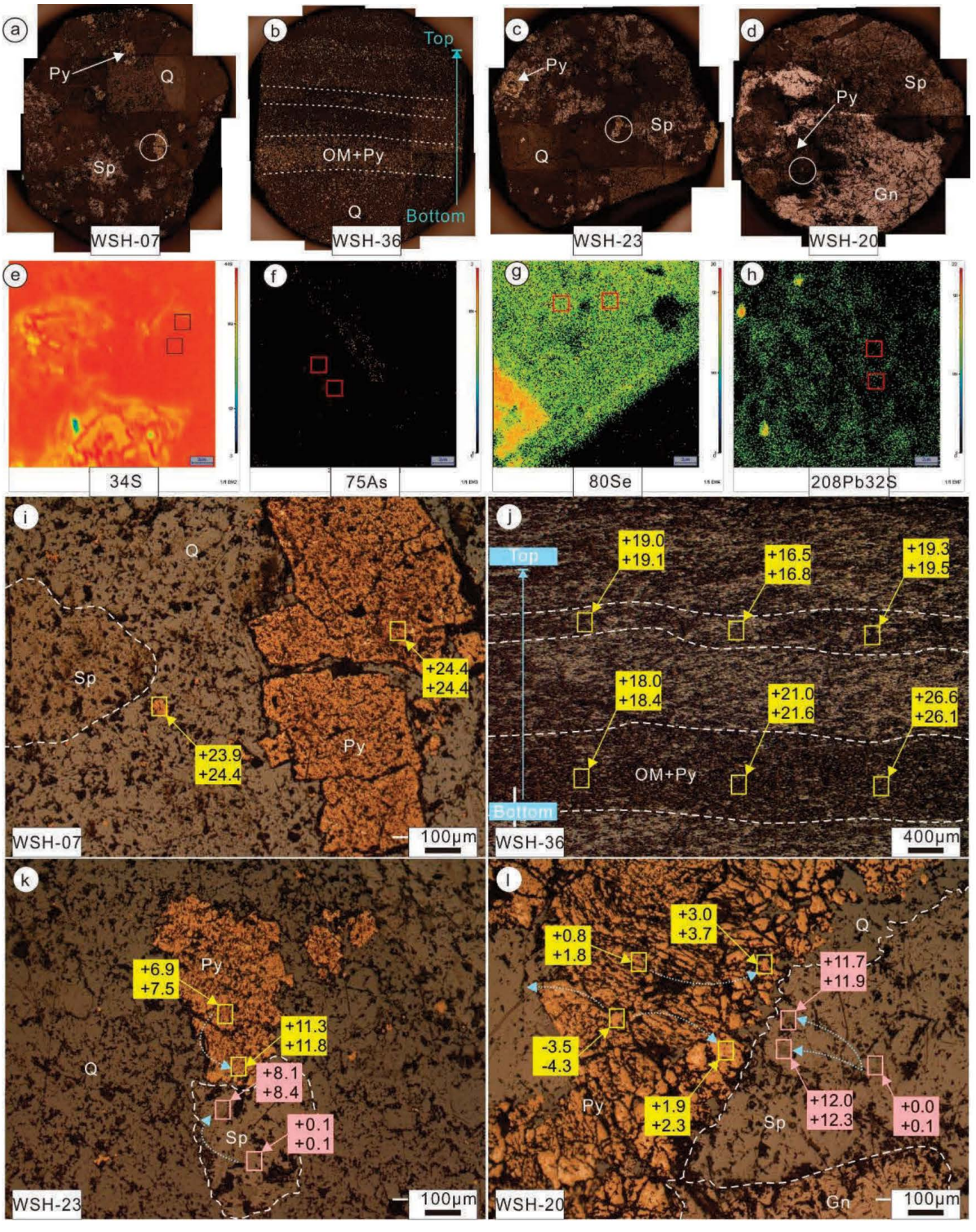

FIGURE 10. Photomicrographs of pyrite and sphalerite from the Wusihe deposit, also showing $\delta^{34}S$ values for spots analyzed by NanoSIMS. (**a**–**d**) Photomicrographs of samples: (**a**) Pyrites occurring in the siliceous dolostones are characterized by fine-grained (<1 mm) euhedral textures; (**b**) abundant fine-grained lamellar pyrite. Thicker organic-rich layers often contain more pyrite; (**c**) pyrite and sphalerite are characterized by fine-grained (<1 mm) subhedral to anhedral textures; (**d**) fine- to coarse-grained massive galena, sphalerite, and pyrite aggregates. (**e**–**h**) Areas selected for in situ S isotope analysis show homogeneous trace element compositions (for example, ^{34}S, ^{75}As, ^{80}Se, $^{208}Pb^{32}S$); (**i**–**l**) photomicrographs showing variation in $\delta^{34}S$ values of sulfide grains from WSH-07, WSH-36, WSH-23, and WSH-20, respectively. Sample numbers correspond to those listed in Supplemental[1] Table S2. Abbreviations: Py = pyrite, Sp = sphalerite, OM = organic matter. (Color online.)

9c, 10k, and 10l), suggesting more ^{32}S-riched H_2S produced by BSR was incorporated during early formation. BSR can only take place at temperatures of <~110 °C (Jorgensen et al. 1992). However, prior to the arrival of hydrothermal fluids, the ambient temperatures during the transition from the late Ediacaran to early Cambrian, were likely <110 °C (Xue et al. 2015). Accordingly, the formation of a local H_2S reservoir prior to the arrival of ore-forming fluids cannot be ruled out. As the temperatures of the mineralizing fluids were episodically raised to more than 120 °C (inferred from fluid inclusion data; e.g., Xiong et al. 2016), the site of mineralization would inhibit BSR and promote TSR. Hence, the mixing of different proportions of H_2S reduced by BSR and TSR is capable of producing the observed range of S isotope values.

Source of metals

As shown in Figure 11a, our new homogeneous Pb isotope data plot above the upper crust evolution line, suggesting a homogeneous or well-mixed metal source originating in the upper crust. Second, the coarse-grained massive galena aggregates have distinct Pb isotopic compositions relative to the fine-grained brecciated and banded sulfide ores (Figs. 11b and 11c). Considering that the U and Th contents of galena are negligible, Pb isotopic ratios of galena formed at different paragenetic stages likely reflect the composition of hydrothermal fluids (Zhou et al. 2018b). The data suggest that the two stages of ore-forming fluids had distinct Pb isotopic compositions (Figs. 11b and 11c). Highly radiogenic Pb from wall rock sequences (e.g., late Ediacaran sedimentary rocks) is inferred to have provided a greater contribution during

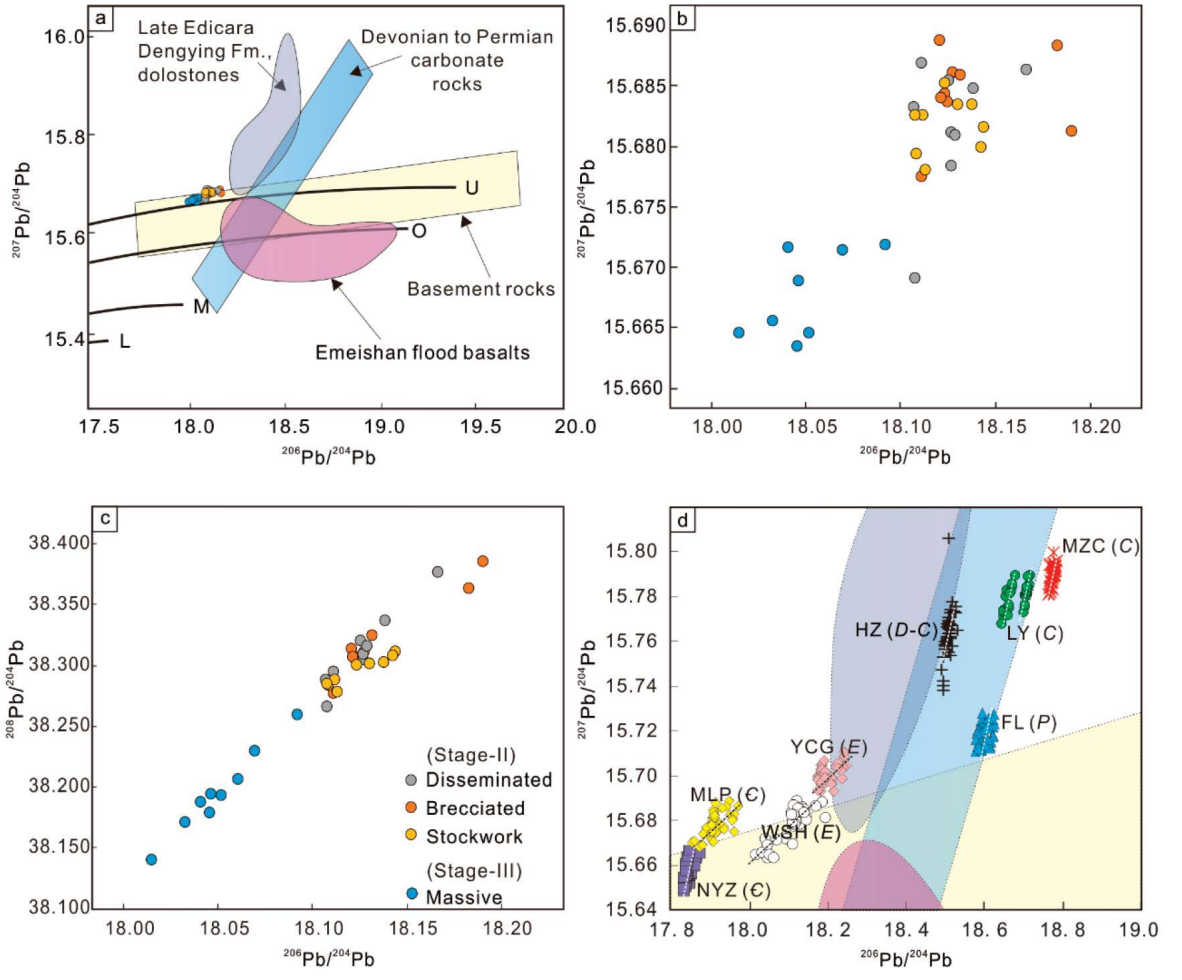

FIGURE 11. (**a**) Comparison plot of Pb isotope ratios $^{207}Pb/^{204}Pb$ vs. $^{206}Pb/^{204}Pb$ among the Wusihe deposit, late Ediacaran Dengying Fm., dolostone, Devonian to Permian carbonate rocks, Proterozoic basement (Kunyang/Huili Group) and late Permian Emeishan basalts (Huang 2004). Data for Upper Continental Crust (U), Orogen Belt (O), Mantle (M), and Lower Continental Crust (L) are from Zartman and Doe (1981). (**b** and **c**) Plots of $^{207}Pb/^{204}Pb$ vs. $^{206}Pb/^{204}Pb$, $^{208}Pb/^{204}Pb$ vs. $^{206}Pb/^{204}Pb$ for galena formed during stage II (disseminated, brecciated, stockwork) and stage III (massive). (**d**) Comparison plot of $^{207}Pb/^{204}Pb$ vs. $^{206}Pb/^{204}Pb$ of in situ data among the Maliping (MLP), Nayongzhi (NYZ), Yinchanggou (YCG), Wusihe (WSH), and Huize (HZ), Fule (FL), (Liangyan) LY, Maozhachang (MZC) deposits (data from Bao et al. 2017, Tan et al. 2017, Zhou et al. 2018a, 2018b, 2018c, and Luo et al. 2019). Letters in brackets represent corresponding sequences hosting the Pb-Zn deposits: *E* = Ediacaran, ε = Cambrian, *D* = Devonian, *C* = Carboniferous, *P* = Permian. Dashed lines represent ages. The data imply that ore formation ages clearly fall into two clusters: (1) Maliping, Wusihe, and Yinchanggou (black lines) and (2) Nayongzhi, Huize, Liangyan, Maozhachang, and Fule (white lines). (Color online.)

stage II mineralization than stage III.

Figure 11d shows the in situ Pb isotopic results from this study, along with previous in situ data from the Upper Yangtze Pb-Zn metallogenic province for comparison (Bao et al. 2017; Tan et al. 2017; Zhou et al. 2018a, 2018b, 2018c; Luo et al. 2019). The data show that in situ Pb isotopic compositions vary between deposits, and that variations correlate directly with the age of the host rock. Galena in situ Pb isotope ratios become increasingly radiogenic from Pb-Zn deposits hosted in Cambrian strata (e.g., the Nayongzhi and Maliping deposits), to those Pb-Zn deposits hosted in Upper Ediacaran strata (e.g., the Wusihe and Yinchanggou deposits), and further still for Pb-Zn deposits in Carboniferous-Permian strata in this province (e.g., the Maozhachang, Liangyan, and Huize deposits). This pattern might have resulted from: (1) the variable accumulation of radiogenic Pb due to variations in parental U and Th concentrations, (2) heterogeneity of the Pb isotopic signature of basement rocks, (3) the evolution (e.g., migration, precipitation) of a single source material (e.g., basement source rocks), or (4) the interaction of separate and isotopically distinct Pb sources (e.g., Moyers 2015; Potra et al. 2018). The first scenario can be excluded because trace element LA-ICPMS data show that there is no significant difference in the U and Th contents of galena among these deposits (Ye et al. 2011 and unpublished data). The slopes may imply that the Maliping, Wusihe, and Yinchanggou deposits are separate from the Nayongzhi, Huize, Liangyan, Maozhachang, and Fule deposits, the two groups defining separate age clusters, supported by radiogenic dating results (dashed lines in Fig. 11d; Wu 2013; Zhang et al. 2014b; Xiong et al. 2018; Zhou et al. 2013b, 2015, 2018a, and references therein). This pattern could potentially result from the evolution of a single source material. However, the fluid driving mechanism in this province during mineralization was considered to be local non-aquifer tectonically driven fluid expulsion from orogenic belts (Han et al. 2007), which is different from that of the Mississippi Valley, or eastern Australia where topographically driven gravitational fluid flow occurred via long-distance/large-scale migration along sandstone aquifers (Appold and Garven 1999; Huston et al. 2017). Our new Pb isotope data plot on the upper margin of the broad field of basement rocks, while Devonian to Permian carbonate rocks extend to significantly more radiogenic compositions (Figs. 11a and 11d). Hence, in addition to Pb isotope variations related to the age of the host rocks, part of the observed scatter may reflect the isotopic heterogeneity of the basement. However, a local mixture of less radiogenic Pb (low $^{207}Pb/^{204}Pb$) from basement rocks and more radiogenic Pb (high $^{207}Pb/^{204}Pb$) originating from carbonate wall rocks cannot be ruled out.

IMPLICATIONS

Ore-forming environments

It is generally accepted that most major low-temperature hydrothermal deposits formed in large-scale contractional events during nearby orogenic activity (e.g., Leach et al. 2010; Hu et al. 2017). These deposits include hydrothermal Hg, Carlin-type Au deposits (e.g., Hu et al. 2017) and the MVT Pb-Zn deposits featured in this study (Fig. 1b; e.g., Zhang 2008; Duan et al. 2014; Xiong et al. 2018; Zhou et al. 2018b). When continental margins in mountain belts are buried beneath thrust sheets, hydrothermal fluids expelled from marginal sediments migrate into the foreland basin and continental interior. These fluids are involved in faulting, migration of hydrocarbons and metals, metamorphism, paleomagnetism, and final ore concentration (Oliver 1986; Appold and Nunn 2005). This environment is consistent with that along the margins of the Yangtze Block (Fig. 1b; e.g., Li et al. 2003; Hu et al. 2017), the formation of low-temperature hydrothermal deposits, occurred in various basin-mountain systems (Fig. 1b), coincided with collision compression and post-collisional extension related to the late Caledonian and the late Indochina orogenies (e.g., Xiong et al. 2018; Zhou et al. 2018b).

In addition to tectonic setting, wall rock sequences appear to be more important in concentrating ores than previously thought. Pb-Zn deposits surrounding the Yangtze Block are primarily hosted in carbonate rocks of the late Ediacaran-early Cambrian and the early Devonian-early Permian (Huang et al. 2004; Zhou et al. 2018b). Among these two sequences, the late Ediacaran Dengying Formation is the dominant host of Pb-Zn orebodies. This is likely because: (1) the Dengying Formation comprises thickly bedded siliceous, evaporitic dolostones with high porosity, interlayered with numerous H_2S-bearing hydrocarbon reservoirs (Shao and Li 1996; Wu et al. 2013; Lin 2014); (2) extensive pre-existing karst cavities and interlayered faulted zones present in this sequence provided the necessary space for the formation of high-grade ores (Lin 2014); and (3) the immediately overlying organic-rich marine black shales of the early Cambrian Qiongzhusi Formation are thermally mature and contain up to 22.3% total organic carbon (TOC), most of which yields type-I kerogen (Zou et al. 2010). The shales provided an important source of oil and hydrocarbons, supported by the large volume of solid bitumen degraded via pyrolysis that characterizes the Wusihe district (e.g., Zhang et al. 2010; Zheng 2012; Luo et al. 2019). Hence, this constitutes an aquitard plus a key geochemical reduction barrier for migrating fluids, for example. This arrangement is in agreement with the occurrence of the ~50 km long ore-hosting belt located in the Wusihe district.

The precipitation mechanism for sulfide minerals

There are three identified precipitation mechanisms for sulfides in MVT deposits, including: (1) the reduced sulfur mechanism; (2) the local sulfate reduction mechanism; and (3) the metal and reduced sulfur-mixing mechanism (Leach et al. 2005 and references therein). At Wusihe, the reduced sulfur mechanism can be excluded because the pH of the predicted mineralizing solution was likely too high (>~5.5) (as suggested by the presence of authigenic K-feldspar), and hence the reduced sulfur and metals were probably not delivered via a single fluid (Sverjensky 1984; Emsbo 2000). The presence of extensive fine-grained and colloform textured sphalerite of stage I indicates a fluid-mixing mechanism in the Wusihe deposit (Fig. 3; Corbella et al. 2004; Zhang et al. 2009). The local sulfate reduction mechanism could dominantly lead to stage II and stage III sulfide precipitation, with typically large, well-formed sulfides reflecting slow H_2S generation, and organic matter derived from ore-hosting wall rocks (Anderson 2015; Xiong et al. 2016).

Evolution of the hydrothermal system

Through an integrated approach, this paper proposes a new working model to explain the Pb-Zn mineralization in the Wusihe

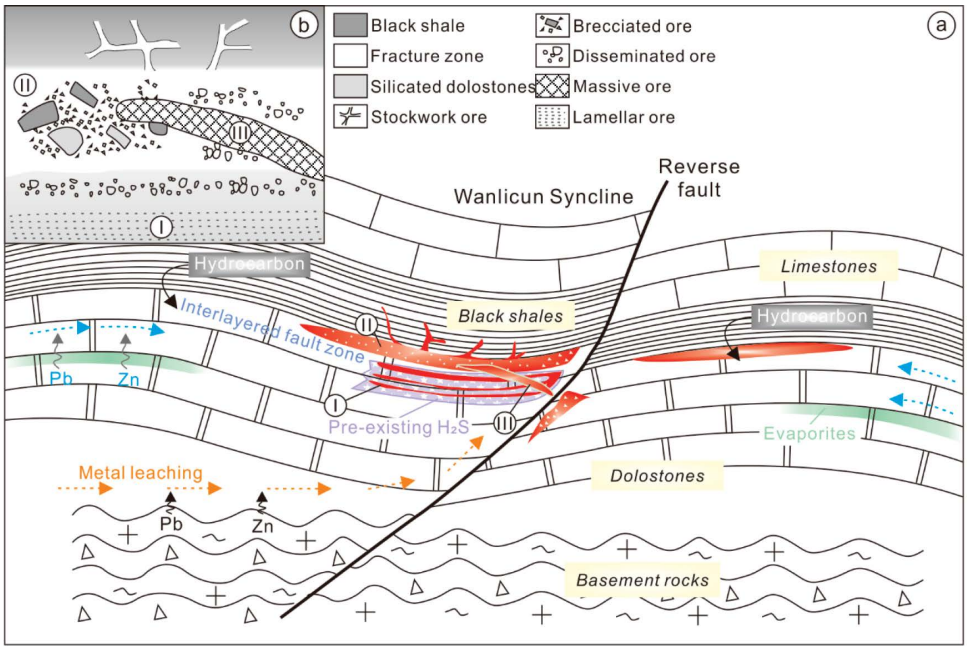

FIGURE 12. (**a**) The ideal model for the evolution of the hydrothermal system in Wusihe, showing metal leaching, fluid mixing, local sulfate reduction and involvement of black shales and carbonate sequences, etc., and (**b**) schematic section showing the deposition of the ores in Wusihe, and the spatial relationship between wall rock sequences and different stages of mineralization (modified from Wang 2015). (Color online.)

district (Fig. 12a). Within the western margin of the Yangtze Block, hot and weakly acidic brines (e.g., $H_2S_{(aq)} + O_{2(aq)} = SO_4^{2-} + 2H^+$; Corbella and Ayora 2003), driven by the late Caledonian orogeny (411 ± 10 Ma; sphalerite Rb-Sr; Xiong et al. 2018), extracted metals primarily from the basement rocks, potentially followed by a limited contribution from local carbonate wall rocks (as suggested by Pb isotopes, this study), to form metal-bearing chloride in ore-forming fluids. These fluids migrated along the Ganluo-Xiaojiang fault zone into unconformities and interlayered fault zones associated with the Wanlicun syncline in the Wusihe district (e.g., Han et al. 2007). This is supported by the presence of authigenic K-feldspar in the Wusihe deposit that required the flux of multiple pore volumes of fluid through the rocks, reflecting fluid migration events during orogenic activity. The fluids interacted with the ^{34}S-enriched pre-existing H_2S generated in situ, largely through close-system BSR (<~110 °C) at the deposition site during the first stage of mineralization (stage I), forming the lower group of the deposition site. Due to variable mineral compositions, porosity, and permeability of the wall rocks, these ore fluids selectively replaced some of the parallel organic-bearing fissure layers in the wall rocks, forming lamellar ores with clear boundaries between sulfide layers.

Meanwhile, a ^{32}S-enriched H_2S reservoir generated by open-system BSR formed before the arrival of the high-*T* ore-forming fluid within the upper group of the deposition site (stage II and stage III; Fig. 12b). The organic-rich Qiongzhusi Formation may have served as a reducing agent. When the fluids ascended, the mineralization system yielded ^{34}S-enriched H_2S because of the high temperature of the fluids inhibited BSR and promoted TSR. Proximal to faults, fluids containing Pb-Zn chloride complexes rapidly mixed with the H_2S reservoir and cooled to form hydrothermal collapse breccia fragments, fine-grained stock-work, and brecciated ores. The relatively Pb-enriched fluids formed massive ore. The sulfide precipitation processes outlined above correspond to an acid-producing chemical reaction (as suggested by Al concentrations). This reaction enhanced the acidity of fluids, resulting in further dissolution of surrounding wall rock carbonates, thereby providing additional space for further sulfide precipitation during ore-forming processes.

ACKNOWLEDGMENTS

We thank Wei Zhou, Gang Xia (The University of Queensland, Australia), En-Tao Liu (China University of Geosciences, Wuhan, China), Tai-Yi Luo, Jun Chen, and Zhen-li Li (Institute of Geochemistry, Chinese Academy of Sciences, China) for fruitful discussions. Comments and suggestions from Fang-Zhen Teng (Associate Editor), Martin Appold, David Huston, and an anonymous reviewer greatly improved the quality of the paper.

FUNDING

This research was financially supported by National Natural Science Foundation of China (41872095 and 41430315), the National Key R&D Program of China (2017YFC0602502), and the Research Start-up Project for Introduced Talent of Yunnan University (YJRC4201804) and the Cultivation Project for Excellent Youth of National Natural Science Foundation of Yunnan University (2018YDJQ009) to J.-X. Zhou.

REFERENCES CITED

Anderson, G. (2015) Kerogen as a source of sulfur in MVT deposits. Economic Geology, 110, 837–840.

Anderson, G., and Macqueen, R. (1982) Ore deposit models-6. Mississippi Valley-type lead-zinc deposits. Geoscience Canada, 9, 108–117.

Appold, M., and Garven, G. (1999) The hydrology of ore formation in the Southeast Missouri district: Numerical models of topography-driven fluid flow during the Ouachita Orogeny. Economic Geology and the Bulletin of the Society of Economic Geologists, 94, 913–935.

Appold, M., and Nunn, J.A. (2005) Hydrology of the Western Arkoma basin and Ozark platform during the Ouachita orogeny: Implications for Mississippi Valley-type ore formation in the Tri-State Zn-Pb district. Geofluids, 5, 308–325.

Bao, Z., Li, Q., and Wang, C.Y. (2017) Metal source of giant Huize Zn-Pb deposit in SW China: New constraints from in situ Pb isotopic compositions of galena. Ore Geology Reviews, 91, 824–836.

Basuki, N.I., Taylor, B.E., and Spooner, E.T.C. (2008) Sulfur isotope evidence for thermochemical reduction of dissolved sulfate in Mississippi Valley-Type zinc-lead mineralization, Bongara Area, Northern Peru. Economic Geology, 103, 783–799.

Chen, X.D., Chen, Z.Y., Cheng, Y.B., Ye, H.S., and Wang, H. (2011) Distribution and Application of Trace Elements in Hydrothermal Quartz: Understanding and prospecting. Geological Review, 57, 707–717 (in Chinese with English abstract).

Chu, Y., Lin, W., Faure, M., Wang, Q.C., and Ji, W.B. (2012) Phanerozoic tectonothermal events of the Xuefengshan Belt, central South China: Implications from U-Pb age and Lu-Hf determinations of granites. Lithos, 150, 243–255.

Corbella, M., and Ayora, C. (2003) Role of fluid mixing in deep dissolution of carbonates. Geologica Acta, 1, pp. 1–305.

Corbella, M., Ayora, C., and Cardellach, E. (2004) Hydrothermal mixing, carbonate dissolution and sulfide precipitation in Mississippi Valley-type deposits. Mineralium Deposita, 39, 344–357.

Crerar, D., Wood, S., Brantley, S., and Bocarsly, A. (1985) Chemical controls on solubility of ore-forming minerals in hydrothermal solutions. Canadian Mineralogist, 23, 333–352.

Duan, Q.F. (2014) The research of metallogenic regularity of stritabound zinc-lead deposits from Sinian-Cambrian in western Hunan and western Hubei. Doctoral dissertation, Chinese Academy of Geological Sciences, Wuhan, pp. 1–156 (in Chinese with English abstract).

Duan, Q.F., Cao, L., Zeng, J.K., Zhou, Y., Tang, C.Y., and Li, K. (2014) Rb-Sr dating of sphalerites from Shizishan Pb-Zn deposit in Huayuan Ore Concentration Area,Western Hunan,and its geological significance. Earth Science, 39, 977–986 and 999 (in Chinese with English abstract).

Durham, K.C. (1966) Role of juvenile solutions, connate waters and evaporitic brines in the genesis of lead zinc-fluorine-barium deposits: Transactions, Institution of Mining and Metallurgy, section B, 75, 226–229.

Emsbo, P. (2000) Gold in sedex deposits. Reviews in Economic Geology, 13, 427–438.

Gibbins, W.A. (1983) Mississippi Valley type lead-zinc districts of northern Canada, In P roceedings, International Conference on Mississippi Valley Type Lead-Zinc Deposits, University of Missouri-Rolla, pp. 403–414.

Götze, J., and Möckel, R. (2012) Quartz: Deposits, mineralogy and analytics. Springer Science & Business Media, pp. 1–360.

Götze, J., Plotze, M., and Habermann, D. (2001) Origin, spectral characteristics and practical applications of the cathodolumimescence (CL) of quartz—a review. Mineralogy and Petrology, 71, 225–250.

Götze, J., Plötze, M., Graupner, T., Hallbauer, D.K., and Bray, C.J. (2004) Trace element incorporation into quartz: A combined study by ICP-MS, electron spin resonance, cathodoluminescence, capillary ion analysis, and gas chromatography. Geochimica et Cosmochimica Acta, 68, 3741–3759.

Guilbert, J.M., and Park, C.F. (1986) The Geology of Ore Deposits, pp. 889–907. W.H. Freeman publication.

Hammerli, J., Spandler, C., Oliver, N.H., Sossi, P., and Dipple, G.M. (2015) Zn and Pb mobility during metamorphism of sedimentary rocks and potential implications for some base metal deposits. Mineralium Deposita, 50, 657–664.

Han, R.S., Liu, C.Q., Huang, Z.L., Chen, J., Ma, D.Y., Lei, L., and Ma, G.S. (2007) Geological features and origin of the Huize carbonate-hosted Zn-Pb-(Ag) District, Yunnan, South China. Ore Geology Reviews, 31, 360–383.

Hou, Z.Q., Wang, S.X., Du, A.D., Qu, X.M., and Sun, W.D. (2003) Re-Os dating of sulfides from the volcanogenic massive sulfide deposit at Gacun, southwestern China. Resource Geology, 53, 305–310.

Hu, R.Z., Fu, S.L., Huang, Y., Zhou, M.F., Fu, S.H., Zhao, C.H., Wang, Y.J., Bi, X.W., and Xiao, J.F. (2017) The giant South China Mesozoic low-temperature metallogenic domain: Reviews and a new geodynamic model. Journal of Asian Earth Sciences, 137, 9–34.

Huang, Z.L., Chen, J., Han, R.S., Li, W.B., Liu, C.Q., Zhang, Z.L., Ma, D.Y., Gao, D.R., and Yang, H.L. (2004) Geochemistry and Ore-formation of the Huize Giant Lead-zinc Deposit, Yunnan, Province, China: Discussion on the Relationship Between Emeishan Flood Basalts and Lead-zinc Mineralization, pp.1–154. Geological Publishing House, Beijing (in Chinese).

Huang, J.L., Zou, C.N., Li, J.Z., Dong, D.Z., Wang, S., Wang, S.Q., and Cheng, K.M. (2012) Shale gas generation and potential of the Lower Cambrian Qiongzhusi Formation in the Southern Sichuan Basin, China. Petroleum Exploration and Development, 39, 75–81.

Huston, D.L., Stevens, B., Southgate, P.N., Muhling, P., and Wyborn, L. (2006) Australian Zn-Pb-Ag ore-forming systems: a review and analysis. Economic Geology, 101, 1117–1157.

Huston, D.L., Champion, D.C., Morrison, G., Maas, R., Thome, J.P., Carr, G., Beams, S., Bottrill, R., Chang, Z.S., Dhnaram, C., and others. (2017) Spatial variations in lead isotopes, Tasman Element, eastern Australia. Geoscience Australia Record, pp. 1–37.

Huttenlocher, H.F. (1935) Crystal structure of aluminium orthophosphate $AlPO_4$. Zeitschrift für Kristallographie, 90, 508–516.

Jiang, Y.H., Jin, G.D., Liao, S.Y., Zhou, Q., and Zhao, P. (2010) Geochemical and Sr–Nd–Hf isotopic constraints on the origin of Late Triassic granitoids from the Qinling orogen, central China: Implications for a continental arc to continent–continent collision. Lithos, 117, 183–197.

Jones, H.D. (1993) Geochemical and sulfur isotopic investigations into the origins of Mississippi Valley-type mineralization in the southern Appalachians and nearby areas. Doctoral dissertation, University of Michigan, pp. 1–279.

Jorgensen, B.B., Isaksen, M.F., and Jannasch, H.W. (1992) Bacterial sulfate reduction above 100°C in deep-sea hydrothermal vent sediments. Science, 258, 1756–1757.

Kong, Z.G., Wu, Y., Liang, T., Zhang, F., Meng, X.Y., and Lu, L. (2017) Sources of ore-forming material for Pb-Zn deposits in the Sichuan-Yunnan-Guizhou triangle area: Multiple constraints from C-H-O-S-Pb-Sr isotopic compositions. Geological Journal, 53, 159–177.

Kucha, H. (2010) Microbial sphalerite formation in carbonate-hosted zn-pb ores, Bleiberg, Austria: micro- to nanotextural and sulfur isotope evidence. Economic Geology, 105, 1005–1023.

Leach, D.L., Sangster, D.F., Kelley, K.D., Large, Ross. R., Garven, G., and Allen, C.R. (2005) Sediment-hosted Pb-Zn Deposits: a global perspective. Economic Geology, 100, 561–608.

Leach, D.L., Bradley, D.C., Huston, D., Pisarevsky, S.A., Taylor, R.D., and Gardoll, S.J. (2010) Sediment-hosted lead-zinc deposits in Earth history. Economic Geology, 105, 593–625.

Leventhal, J.S. (1990) Organic matter and thermochemical sulfate reduction in the viburnum trend, Southeast Missouri. Economic Geology, 85, 622–632.

Li, T.Z. (2007) The genesis and metallogenic model oflead-zinc deposits in the middle part of Dadu River Valley. Master dissertation, Chengdu Institute of Technology, Chengdu, China, pp. 1–55 (in Chinese with English abstract).

Li, X.H., Li, Z.X., Li, W.X., and Wang, Y. (2006) Initiation of the Indosinian Orogeny in South China: evidence for a Permian magmatic arc on Hainan Island. The Journal of Geology, 114, 341–353.

Li, J.W., Vasconcelos, P., Zhou, M.F., Deng, X.D., Cohen, B., Bi, S.J., Zhao, X.F., and Selby, D. (2014) Longevity of magmatic–hydrothermal systems in the Daye Cu–Fe–Au District, eastern China with implications for mineral exploration. Ore Geology Reviews, 57, 375–392.

Li, Y., He, D., Li, D., Lu, R., Fan, C., Sun, Y., and Huang, H. (2018) Sedimentary provenance constraints on the Jurassic to Cretaceous paleogeography of Sichuan Basin, SW China. Gondwana Research, 60, 15–33.

Lin, F.C. (2005) Geological and geochemical characteristics and genesis of super-large-scale Sedex-type stratiform lead-zinc deposits in the Dadu River Valley on the western margin of the Yangtze Craton. Acta Geologica Sinica, 79, 540–556 (in Chinese with English abstract).

Lin, X.X. (2014) Study on dolomite and metallogenic regularity of lead-zinc deposits within the Sinian Dengying Formation in Hanyuan region, Sichuan Province, China. Doctoral dissertation, Chengdu Institute of Technology, Chengdu, China, pp. 154 (in Chinese with English abstract).

Liu, H.C., and Lin, W.D. (1999) Study on the Pb–Zn–Ag ore deposits in northeast Yunnan, Yunnan, China. Yunnan University Press, Kunming, pp. 1–468 (in Chinese).

Lu, S., Li, H., Chen, Z., Hao, G., Zhou, H., Guo, J., Niu, G., and Xiang, Z. (2003) Meso-Neoproterozoic geological evolution in the Qinling orogeny and its response to the supercontinental events of Rodinia. Geological Publish House, Beijing: pp. 1–194.

Luo, K., Zhou, J.X., Huang, Z.L., Wang, X.C., Wilde, S.A., Zhou, W., and Tian, L. (2019) New insights into the origin of early Cambrian carbonate-hosted Pb-Zn deposits in South China: A case study of the Maliping Pb-Zn deposit. Gondwana Research, 70, 88–103.

Machel, H.G., Krouse, H.R., and Sassen, R. (1995) Products and distinguishing criteria of bacterial and thermochemical sulfate reduction. Appllied Geochemistry, 10, 373–389.

Mackey, J.H. (1963) EPR study of impurity-related color centers in germanium-doped quartz. Journal of Chemical Physics, 39, 74–83.

Mi, M., Chen, Y.J., Yang, Y.F., Wang, P., Li, F.L., Wan, S.Q., and Xu, Y.L. (2015) Geochronology and geochemistry of the giant Qian'echong Mo deposit, Dabie Shan, eastern China: Implications for ore genesis and tectonic setting. Gondwana Research, 27, 1217–1235.

Moyers, A. (2015) Source Constraints of Ore Metals In Mississippi Valley-Type Deposits in Central and Eastern Tennessee Using Pb Isotopes. Master dissertation, University of Arkansas. pp. 1–76.

Ohmoto, H. (1972) Systematics of sulfur and carbon isotopes in hydrothermal ore deposits. Economic Geology, 67, 551–578.

——— (1986) Stable isotope geochemistry of ore-deposits. Reviews in Mineralogy, 16, 491–559.

Ohmoto, H., and Rye, R. (1979) Isotopes of sulfur and carbon. Geochemistry of Hydrothermal Ore Deposits, 509–567.

Oliver, J. (1986) Fluids expelled tectonically from orogenic belts: Their role in hydrocarbon migration and other geologic phenomena. Geology, 14, 99–102.

Paradis, S., Hannigan, P., and Dewing, K. (2007) Mississipi valley-type lead-zinc deposits (MVT). Mineral deposits of Canada, Geological Survey of Canada, p. 1–15.

Peevler, J., Fayek, M., Misra, K.C., and Riciputi, L.R. (2003) Sulfur isotope microanalysis of sphalerite by SIMS: constraints on the genesis of Mississippi valley-type mineralization, from the Mascot-Jefferson City district, East Tennessee. Journal of Geochemical Exploration, 80, 277–296.

Perny, B., Eberhardt, P., Ramseyer, K., Mullis, J., and Pankrath, R. (1992) Microdistribution of Al, Li, and Na in α quartz: possible causes and correlation with short-lived cathodoluminescence. American Mineralogist, 77, 534–544.

Potra, A., Garmon, W.T., Samuelsen, J.R., Wulff, A., and Pollock, E.D. (2018) Lead isotope trends and metal sources in the Mississippi Valley-type districts from the mid-continent United States. Journal of Geochemical Exploration, 192, 174–186.

Rusk, B.G., Lowers, H.A., and Reed, M.H. (2008) Trace elements in hydrothermal quartz: Relationships to cathodoluminescent textures and insights into vein formation. Geology, 36, 547–550.

Shao, S.C., and Li, C.Y. (1996). Metallogenetic rules of the strata-bound Pb-Zn deposit in Dengying Formation of the west margin of Yangtze massif and its possibility of ore-forming super-large ore deposit. Yunnan Geology, 15, 345–350 (in Chinese with English abstract).

Shu, L.S. (2006) Predevonian tectonic evolution of south China: from Cathaysian Block to Caledonian period folded orogenic belt. Geological Journal of China Universities, 12, 418–431.

Sverjensky, D.A. (1981) The origin of a Mississippi Valley-type deposit in the Viburnum Trend, Southeast Missouri. Economic Geology, 76, 1848–1872.

———(1984) Oil field brines as ore-forming solutions. Economic Geology, 79, 23–37.

Talluri, J.K., Pandalai, H.S., and Jadhav, G.N. (2000) Fluid chemistry and depositional mechanism of the epigenetic, discordant ores of the proterozoic, carbonate-hosted, Zawarmala Pb-Zn Deposit, Udaipur District, India. Economic Geology, 95, 1505–1525.

Tan, S.C., Zhou, J.X., Li, B., and Zhao, J.X. (2017) In situ Pb and bulk Sr isotope analysis of the Yinchanggou Pb-Zn deposit in Sichuan Province (SW China): Constraints on the origin and evolution of hydrothermal fluids. Ore Geology Reviews, 91, 432–443.

Wang, X.H., Xue, C.J., Li, Z.M., Li, Q., and Yang, R.J. (2008) Geological and geochemical characteristics of Mayuan Pb-Zn ore deposit on northern margin of Yangtze landmass. Mineral Deposits, 27, 37–48 (in Chinese with English abstract).

Wang, Y.J., Zhang, F.F., Fan, W.M., Zhang, G.W., Chen, S.Y., Cawood, P.A., and Zhang, A.M. (2010) Tectonic setting of the South China Block in the early Paleozoic: Resolving intracontinental and ocean closure models from detrital zircon U-Pb geochronology. Tectonics, 29, TC6020, doi: 10.1029/2010TC002750.

Wang, L.J., Yu, J.H., Griffin, W.L., and O'Reilly, S.Y. (2012) Early crustal evolution in the western Yangtze Block: Evidence from U–Pb and Lu–Hf isotopes on detrital zircons from sedimentary rocks. Precambrian Research, 222–223, 368–385.

Wang, C.M., Deng, J., Carranza, E.J.M., and Lai, X.R. (2014) Nature, diversity and temporal–spatial distributions of sediment-hosted Pb–Zn deposits in China. Ore Geology Reviews, 56, 327–351.

Wang, W. (2015) Texture and structure characteristics of ore and genetic research of Wusihe Pb-Zn deposit, Sichuan Province. Master dissertation, China University of Geosciences. Beijing, pp. 1–56 (in Chinese with English abstract).

Wilkinson, J. (2013) Sediment-hosted zinc-lead mineralization: Processes and perspectives. In H. Holland and K. Turekian, Eds., Processes and Perspectives, Treatise on Geochemistry, Elsevier, Amsterdam, Netherlands, pp. 219–249. Doi:10.1016/B978-0-08-095975-7.01109-8.

Wilkinson, J.J., Eyre, S.L., and Boyce, A.J. (2005) Ore-forming processes in Irish-type carbonate-hosted Zn-Pb deposits: Evidence from mineralogy, chemistry, and isotopic composition of sulfides at the Lisheen mine. Economic Geology, 100, 63–86.

Wu, Y. (2013) The age and ore-forming process of MVT deposits in the boundary area of Sichuan-Yunnan-Guizhou provinces, Southwest China. Doctoral dissertation, China University of Geosciences. Beijing, pp. 1–175 (in Chinese with English abstract).

Wu, Y., Zhang, C.Q., Mao, J.W., Ouyang, H.G., and Sun, J. (2013) The genetic relationship between hydrocarbon systems and Mississippi Valley-type Zn-Pb deposits along the SW margin of Sichuan Basin, China. International Geology Review, 55, 941–957.

Wu, T., Zhou, J.X., Wang, X.C., Li, W.X., Wilde, S.A., Sun, H.R., Wang, J.S., and Li, Z. (2018) Identification of ca. 850 Ma high-temperature strongly peraluminous granitoids in southeastern Guizhou Province, South China: A result of early extension along the southern margin of the Yangtze Block. Precambrian Research, 308, 18–34.

Xiong, S.F., Yao, S.Z., Gong, Y.J., Tang, M.T., Zeng, G.P., and Wang, W. (2016) Ore-forming fluid and thermochemical sulfate reduction in the Wusihe lead-zinc deposit, Sichuan Province, China. Earth Science 41, 105–120 (in Chinese with English abstract).

Xiong, S.F., Gong, Y.J., Jiang, S.Y., Zhang, X.J., Li, Q., and Zeng, G.P. (2018) Ore genesis of the Wusihe carbonate-hosted Zn-Pb deposit in the Dadu River Valley district, Yangtze Block, SW China: evidence from ore geology, S-Pb isotopes, and sphalerite Rb-Sr dating. Mineralium Deposita, 53, 967–979.

Xue, C., Chi, G., and Fayek, M. (2015) Micro-textures and in situ sulfur isotopic analysis of spheroidal and zonal sulfides in the giant Jinding Zn–Pb deposit, Yunnan, China: Implications for biogenic processes. Journal of Asian Earth Sciences, 103, 288–304.

Ye, L., Cook, N.J., Ciobanu, C.L., Yuping, L., Qian, Z., and Tiegeng, L. (2011) Trace and minor elements in sphalerite from base metal deposits in south china: a LA-ICPMS study. Ore Geology Reviews, 39, 188–217.

Yuan, S.D., Ellis, G.S., Chou, I.M., and Burruss, R.C. (2017) Experimental investigation on thermochemical sulfate reduction in the presence of 1-pentanethiol at 200 and 250°C: Implications for in situ TSR processes occurring in some MVT deposits. Ore Geology Reviews, 91, 57–65.

Zartman, R.E., and Doe, B.R. (1981) Plumbotectonics—the model. Tectonophysics, 75, 135–162.

Zhang, C.Q. (2008) The genetic model of Mississippi Valley-type deposits in the boundary area of Sichuan, Yunnan and Guizhou Province, China. Doctoral dissertation, Chinese Academy of Geological Sciences, Beijing, pp. 1–167 (in Chinese with English abstract).

Zhang, S.B., Zheng, Y.F., Wu, Y.B., Zhao, Z.F., Gao, S., and Wu, F.Y. (2006) Zircon U-Pb age and Hf-O isotope evidence for Paleoproterozoic metamorphic event in South China. Precambrian Research, 151, 265–288.

Zhang, C.Q., Li, X.B., Yu, J.J., Mao, J.W., Chen, F.K., and Li, H.M. (2008) Rb–Sr dating of single sphalerites from the Daliangzi Pb–Zn deposit, Sichuan, and its geological significances. Geological Review, 54, 145–151 (in Chinese with English abstract).

Zhang, C.Q., Yu, J.J., Mao, J.W., and Rui, Z.Y. (2009) Advances in the study of Mississippi Valley-type deposits. Mineral deposits, 28, 195–210 (in Chinese with English abstract).

Zhang, C.Q., Yu, J.J., Mao, J.W., Yu, H., and Li, H.M. (2010) Research on the Biomarker from Chipu Pb-Zn Deposit, Sichuan. Acta Sedimentologica Sinica, 28, 832–844 (in Chinese with English abstract).

Zhang, G.W., Guo, A.L., Wang, Y.J., Li, S.Z., Dong, Y.P., Liu, S.F., He, D.F., Cheng, S.Y., Lu, R.K., and Yao, A.P. (2013) Tectonics of South China continent and its implications. Science China Earth Sciences, 56, 1804–1828.

Zhang, C.Q., Wu, Y., Wang, D.H., and Chen, Y.C. (2014a) Brief introducition on metallogeny of Pb-Zn deposits in China. Acta Geologica Sinica, 88, 2252–2268 (in Chinese with English abstract).

Zhang, Y.X., Wu, Y., Tian, G., Shen, L., Zhou, Y.M., Dong, W.W., Zeng, R., Yang, X.C., and Zhang, C.Q. (2014b) Mineralization Age and the Source of Ore-forming Material at Lehong Pb-Zn Deposit, Yunnan Province: Constraints from Rb-Sr and S Isotopes System. Acta Mineralogica Sinica, 34, 305–311 (in Chinese with English abstract).

Zhao, G.C. (2015) Jiangnan Orogen in South China: Developing from divergent double subduction. Gondwana Research, 27, 1173–1180.

Zhao, X.F., Zhou, M.F., Li, J.W., Sun, M., Gao, J.F., Sun, W.H., and Yang, J.H. (2010) Late Paleoproterozoic to early Mesoproterozoic Dongchuan Group in Yunnan, SW China: Implications for tectonic evolution of the Yangtze Block. Precambrian Research, 182, 57–69.

Zhao, J.H., Zhou, M.F., Yan, D.P., Zheng, J.P., Li, and J.W. (2011) Reappraisal of the ages of Neoproterozoic strata in South China: No connection with the Grenvillian orogeny. Geology, 39, 299–302.

Zheng, X.Z. (2012) Geological features and genesis of Wusihe Pb-Zn deposit, Sichuan. Master dissertation, Chang'an University, Xi'an, China, pp. 1–66 (in Chinese with English abstract).

Zhou, M.F., Yan, D.P., Kennedy, A.K., Li, Y.Q., and Ding, J. (2002) SHRIMP U-Pb zircon geochronological and geochemical evidence for Neoproterozoic arc-magmatism along the western margin of the Yangtze Block, South China. Earth and Planetary Science Letters, 196, 51–67.

Zhou, M.F., Ma, Y.X., Yan, D.P., Xia, X.P., Zhao, J.H., and Sun, M. (2006) The Yanbian terrane (Southern Sichuan Province, SW China): A neoproterozoic are assemblage in the western margin of the Yangtze block. Precambrian Research, 144, 19–38.

Zhou, J.C., Wang, X.L., and Qiu, J.S. (2009) Geochronology of Neoproterozoic mafic rocks and sandstones from northeastern Guizhou, South China: Coeval arc magmatism and sedimentation. Precambrian Research, 170, 27–42.

Zhou, J.X., Huang, Z.L., and Yan, Z.F. (2013a) The origin of the Maozu carbonate-hosted Pb-Zn deposit, southwest China: Constrained by C-O-S-Pb isotopic compositions and Sm-Nd isotopic age. Journal of Asian Earth Sciences, 73, 39–47.

Zhou, J.X., Huang, Z.L., Zhou, M., Li, X., and Jin, Z.G. (2013b) Constraints of C-O-S-Pb isotope compositions and Rb-Sr isotopic age on the origin of the Tianqiao carbonate-hosted Pb-Zn deposit, SW China. Ore Geology Reviews, 53, 77–92.

Zhou, J.X., Bai, J.H., Huang, Z.L., Zhu, D., Yan, Z.F., and Lv, Z.C. (2015) Geology, isotope geochemistry and geochronology of the Jinshachang carbonate-hosted Pb–Zn deposit, southwest China. Journal of Asian Earth Sciences, 98, 272–284.

Zhou, J.X., Luo, K., Wang, X.C., Wilde, S.A., Wu, T., Huang, Z.L., Cui, Y.L., and Zhao, J.X. (2018a) Ore genesis of the Fule Pb-Zn deposit and its relationship with the Emeishan Large Igneous Province: Evidence from mineralogy, bulk C-O-S and in situ S-Pb isotopes. Gondwana Research, 54, 161–179.

Zhou, J.X., Wang, X.C., Wilde, S.A., Luo, K., Huang, Z.L., Wu, T., and Jin, Z.G. (2018b) New insights into the metallogeny of MVT Zn-Pb deposits: A case study from the Nayongzhi in South China, using field data, fluid compositions, and in situ S-Pb isotopes. American Mineralogist, 103, 91–108.

Zhou, J.X., Xiang, Z.Z., Zhou, M.F., Feng, Y.X., Luo, K., Huang, Z.L., and Wu, T. (2018c) The giant Upper Yangtze Pb-Zn province in SW China: Reviews, new advances and a new genetic model. Journal of Asian Earth Sciences, 154, 280–315.

Zhu, C.W., Liao, S.L., Wang, W., Zhang, Y.X., Yang, T., Fan, H.F., and Wen, H.J. (2018) Variations in Zn and S isotope chemistry of sedimentary sphalerite, Wusihe Zn-Pb deposit, Sichuan Province, China. Ore Geology Reviews, 95, 639–648.

Zou, C.N., Dong, D.Z., Wang, S.J., Li, J.Z., Li, X.J., Wang, Y.M., Li, D.H., and Cheng, K.M. (2010) Geological characteristics and resource potential of shale gas in China. Petroleum Exploration and Development, 37, 641–653.

Manuscript received May 1, 2019
Manuscript accepted August 25, 2019
Manuscript handled by Fang-Zhen Teng

Endnote:

[1]Deposit item AM-20-17021, Supplemental Material. Deposit items are free to all readers and found on the MSA website, via the specific issue's Table of Contents (go to http://www.minsocam.org/MSA/AmMin/TOC/2020/Jan2020_data/Jan2020_data.html).